

Contents

1	Introduction	3
2	Theoretical background	5
2.1	The nuclear shell model	5
2.1.1	A shell model calculation code - ANTOINE	9
2.1.2	Interactions	10
2.1.3	The Coulomb energy	11
2.2	Electromagnetic Transitions	11
2.2.1	Transition probability	12
2.2.2	Branching ratios	13
2.2.3	Mixing ratio	14
2.3	Prompt particle decay	14
3	Experimental technique	17
3.1	Experimental method	17
3.2	Experimental set-up	19
3.2.1	Gammasphere	19
3.2.2	Ancillary detectors	20
3.3	The experiments and data handling	23
4	The doubly magic nucleus ^{56}Ni	27
4.1	Experimental results	27
4.1.1	Coincidence spectroscopy	27
4.1.2	Spin and parity assignments	30
4.2	Shell model interpretation	32
4.2.1	Level energies	32
4.2.2	Occupation number	34
4.2.3	Pure particle hole excitations	35
4.2.4	Coulomb effects	37
4.2.5	Transition probabilities	39
5	The Lund University Silicon Array	47
5.1	The strip detectors	47
5.2	Detector arrangement	48
5.3	Electrical set-up	51
5.4	Determination of the angles of the pixels	52
5.5	The alpha calibration	54

5.6	Proton Calibration	56
5.6.1	Determination of the proton energy	56
5.6.2	The beam energy	59
5.6.3	Spectra	61
5.6.4	Calibration	63
5.6.5	Absorber foils	64
5.7	Evaluation of the calibration	65
6	Conclusions and Outlook	69
	Acknowledgements	71
	References	74

Chapter 1

Introduction

The atomic nucleus is a very small object, its only about 10^{-12} cm in diameter. Still it is the object which dominates the world around us. Hydrogen and helium nuclei were created within the first minute of the Universe after the Big Bang some 14 billion years ago. The primordial universe expanded and lumps of hydrogen and helium were pulled together by the gravitational force. As the hydrogen and helium nuclei were pulled closer and closer together, they could fuse together forming heavier nuclei. The lumps of hydrogen and helium became stars. Remarkably, the mass of the constituents is greater than the mass of the fused system. The excess mass is converted into energy according to $E = mc^2$. The energy can be carried away by a photon, a massless particle which we see as light. Looking up at the night sky, twinkling with stars, what we see are the photons created from fusion inside the stars. All elements on earth were created in the life cycle of stars. Hence, to study nuclei is to study the very foundation of us, the Earth, and the evolution of the Universe.

The atomic nucleus is a many body quantal system, consisting of strongly interacting fermions: protons and neutrons. Its properties are governed by the interplay between the strong, weak, and electromagnetic forces. Nuclei can thus display a plethora of interesting and diverse phenomena. The Nobel price in physics was awarded to Maria Goeppert-Mayer and Hans Jensen in 1963 for their shell-model description of the nucleus. In that mean field model, every neutron and proton inside the nucleus experiences an average force due to all the other nucleons. This means that every nucleon occupies a defined state, which has a specific set of quantum numbers associated with it. Goeppert-Mayer explained why some nuclei with certain numbers of protons and neutrons are more stable than the neighbouring nuclei. These are now known as the 'magic numbers': 2, 8, 20, 28, 50, and 82. The numbers represent the closing of major shells. The term "magic numbers" was invented by Eugene Wigner to indicate his disbelief in the phenomenon [1] but by now the magic numbers are well established both experimentally and theoretically.

In this thesis the doubly magic nucleus ${}^{56}_{28}\text{Ni}_{28}$ is studied. The ground state of ${}^{56}\text{Ni}$ is supposed to be formed by a closed proton and neutron shell. However, contemporary state-of-the-art shell model calculations indicate that the closed shell structure is not dominating the ground state of ${}^{56}\text{Ni}$. The energy of the first excited

state in ^{56}Ni is much lower compared to other doubly magic nuclei, as is the transition probability from the first excited state to the ground state. ^{56}Ni is thus an interesting nucleus to study as it does not behave like a 'typical' magic nucleus.

The first paper discusses ^{56}Ni .

- **Gamma-ray spectroscopy of the doubly magic nucleus ^{56}Ni**

E. K. Johansson, D. Rudolph, J. Ekman, C. Fahlander, C. Andreoiu, M.A. Bentley, M. P. Carpenter, R.J. Charity, R.M. Clark, P. Fallon, R. V. F. Janssens, F.G. Kondev, T.L. Khoo, T. Lauritsen, A.O. Macchiavelli, W. Reviol, D.G. Sarantites, D. Seweryniak, C.E. Svensson, and S. J. Williams.

Eur. Phys. J. A **27**, 157-165 (2006).

In Sec. 3 the experimental method to produce $^{56}_{28}\text{Ni}_{28}$ is described. The analysis of the experimental data and its interpretation is discussed in Sec. 4 within the theoretical framework outlined in Sec. 2.

A new exciting decay mode has been discovered in neutron deficient exotic nuclei in the mass $A \sim 60$ region. Since its first observation in ^{58}Cu it has been observed in several nuclei. A highly deformed excited nuclear state usually decays by emitting γ -rays but ^{58}Cu instead decays by emitting a proton. The daughter nucleus is nearly spherical. Thus in the process of proton emission the mother nucleus drastically rearranges its shape and hence its potential. The proton has to tunnel through the potential barrier to escape the nucleus. By measuring the properties of these protons, insights into the tunnelling process may be achieved. To accurately measure the protons a charged particle detector array - the LuSiA - was constructed.

Paper 2 deals with prompt proton decays in the $A \sim 60$ region and LuSiA;

- **Proton decay in the $A \sim 60$ region**

E. K. Johansson, D. Rudolph, R. Hoischen, L-L. Andersson, R. du Rietz, J. Ekman, C. Fahlander, C. Andreiou, M. Carpenter, R. J. Charity, C. J. Chiara, C. Hoel, O. L. Pechenaya, W. Reviol, D. G. Sarantites, D. Seweryniak, L.G. Sobotka, D. Torres, S. Zhu, M. Hellström, S. Pietri, Zs. Podolyák, P.H. Regan, F. Becker, P. Bednarczyk, L. Caceres, P. Doornenbal, J. Gerl, M. Górska, J. Grębosz, I. Kojouharov, N. Kurz, W. Prokopowicz, H. Schaffner, H.J. Wollersheim, L. Atanasova, D.L. Balabanski, M.A. Bentley, C. Brandau, J. Brown, A.B. Garnsworthy, and A. Jungclaus.

Nuclear Structure '06, conference on nuclei at the limits, proceedings, to be published.

The experiment in which LuSiA was used is described in Sec. 3.3 and the calibration of it is discussed in detail in Sec. 5. The thesis finishes with some conclusions and an outlook (Sec. 6).

Chapter 2

Theoretical background

2.1 The nuclear shell model

It is an experimental fact that atomic nuclei exhibit a shell structure. For instance, along the line of stability the proton separation energies show large discontinuities for certain proton numbers; 2, 8, 20, 28, 50, and 82. These are the so called magic numbers. For neutrons one additional magic number is known; 126. The magic numbers represent the closing of major shells and with the discovery of them came the desire to describe the nucleus in an analogous way to the atom. However, significant differences exist between the nuclear shells and the atomic shells. The electrons move in an attractive Coulomb potential created by the nucleus, whereas the protons and neutrons move in a potential created by themselves. It implies for nucleons that there is no 'independent' center of the force, like in the atomic case. The nuclear potential is created from the strong, the Coulomb and the weak forces. It is assumed that the nucleons move independently of each other in the nucleus. The independent motion is motivated by the short range nature of the strong force and the Pauli exclusion principle; only one spin-1/2 particle is allowed to occupy a certain quantum state at a given time. When trying to theoretically describe nuclei two major problems arise; (i) the nucleus is a many body system, but not even the classical three body system is exactly solvable, and (ii) the nucleon-nucleon interaction is not well understood.

The starting point for a theoretical model to describe nuclei is to solve the Schrödinger equation

$$H\Psi = E\Psi$$

where the Hamiltonian, for an A nucleon system, is given by

$$H = \sum_{i=1}^A \left(-\frac{\hbar^2}{2m} \nabla_i^2 \right) + \frac{1}{2} \sum_{j,i=1}^A V_{ij}(\vec{r}_i, \vec{r}_j)$$

The first term of the Hamiltonian describes the kinetic energy of the nucleons. A two body interaction between the nucleons is described by the second term. As the nucleon-nucleon interaction is not completely understood, no exact form for the last term in the Hamiltonian exists. To handle this problem in practice, the Hamiltonian

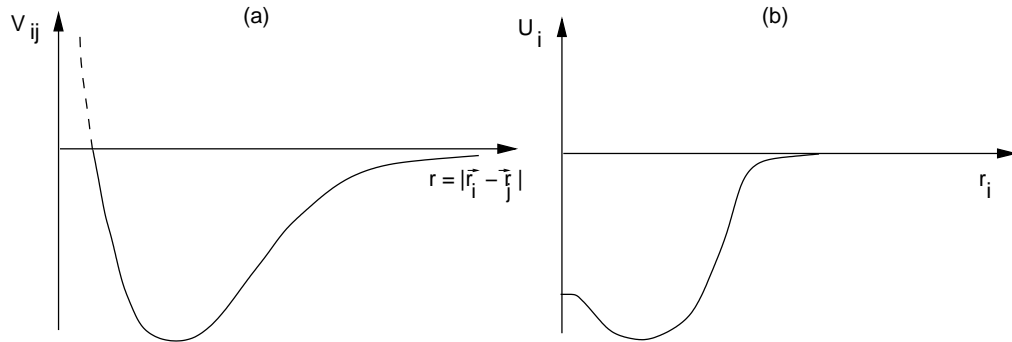


Figure 2.1: (a) The two-body interaction V_{ij} in a nucleus, is repulsive (attractive) at short (long) distances between the nucleons. (b) The average one body potential, is used to approximate the two body interaction. Picture inspired by Ref. [2].

is divided into

$$H = H_0 + H_{res} \quad (2.1)$$

where

$$H_0 = \sum_{i=1}^A \left(-\frac{\hbar^2}{2m} \nabla_i^2 + U_i \right)$$

and

$$H_{res} = \frac{1}{2} \sum_{i,j=1}^A V_{ij}(\vec{r}_i, \vec{r}_j) - \sum_{i=1}^A U_i$$

where H_0 describes the motion of A nucleons, independent of each other in the same average field, U_i . The residual interaction is described by H_{res} , the smaller the effect of it, the better the assumption of an average independent field becomes. In Fig. 2.1 the difference between the two potentials is schematically shown. The V_{ij} potential is repulsive at short distances between the two particles, reflecting the behaviour of the strong force. The U_i potential on the other hand is attractive for all distances, inside the nucleus. It also utilises the short range of the strong force, in that the central potential is proportional to the density distribution of the nucleus. A commonly used central potential is the Woods-Saxon potential

$$U_{WS}(r) = \frac{-V_0}{1 + e^{\frac{r-R}{a}}}$$

where V_0 is the depth of the potential well, R is the nuclear radius, and a is the skin diffuseness parameter. Typically the depth of the well, V_0 , is 50 MeV and a is 0.55 fm. For normal nuclear matter the radius, R , is given by $R = 1.3 \cdot A^{1/3}$, where A is the mass number of the nucleus. This approximation of the nuclear radius is based on the assumption that the nucleus is spherical. Thus this model is valid for spherical nuclei.

For a central potential the Schrödinger equation can be separated into a radial and an angular part, which are independent of each other. To solve the angular

part, the orbital angular quantum number, ℓ , is introduced through

$$\vec{\ell}^2|\psi\rangle = \ell(\ell + 1)\hbar^2|\psi\rangle$$

where ψ is the single-particle wave function. ℓ can only take integer values, denoted s, p, d , etc. corresponding to $\ell = 0, 1, 2$, etc. Connected to the orbital angular momentum is the quantum number parity, π . It gives the symmetry of a wave function if its space coordinates are changed from $\mathbf{r} \rightarrow -\mathbf{r}$. The parity is determined by $\pi = (-1)^\ell$. Hence orbitals with an even (odd) orbital angular quantum number have a positive (negative) parity.

The orbital angular momentum vector has different orientations in space with respect to the quantisation axis, z . The projection of $\vec{\ell}$ on the z -axis is given by

$$\ell_z|\psi\rangle = m_\ell\hbar|\psi\rangle$$

m_ℓ takes integer values from $-\ell, \dots, \ell$. The protons and neutrons have an intrinsic spin, \vec{s} , of $1/2$ as discussed earlier, its projection on the z -axis is given by

$$s_z|\psi\rangle = m_s\hbar|\psi\rangle$$

The number of particles that can occupy a given shell is given by

$$2(2\ell + 1)$$

where the factor $(2\ell + 1)$ is the degeneracy in m_ℓ and the factor 2 corresponds to the two spin directions of the intrinsic spin. The energy levels obtained using the Woods-Saxon potential are shown in panel (a) of Fig. 2.2. The notation is given in $n\ell$, where n is the number of levels for a given ℓ orbital and the numbers in the circles are the theoretical magic numbers. Evidently the experimental magic numbers beyond 20 are not reproduced by this model.

To properly recreate the experimentally observed magic numbers it is necessary to add a spin-orbit interaction into the Woods-Saxon potential

$$U_{WS+SO} = \frac{-V_0}{1 + e^{\frac{r-R}{a}}} + U_{SO}(r)\vec{\ell} \cdot \vec{s}.$$

This was discovered by Goeppert-Mayer in 1949 [3]. The spin-orbit interaction couples the orbital angular momentum, ℓ , to the intrinsic spin, s , through

$$\vec{j} = \vec{\ell} + \vec{s}$$

The quantum number j is associated with \vec{j} , and the projection on the quantisation axis is given by

$$m_j = m_\ell + m_s$$

The effects from adding the spin-orbit interaction can be seen in panel (b) of Fig. 2.2. The spin orbit interaction breaks the degeneracy of $\ell \geq 0$ levels into a $j = \ell + s$ level and a $j = \ell - s$ level. The levels with $j = \ell + s$ are lowered in energy, clearly seen in Fig. 2.2 panel (b). The levels in panel (b) are denoted according to $n\ell j$, and the

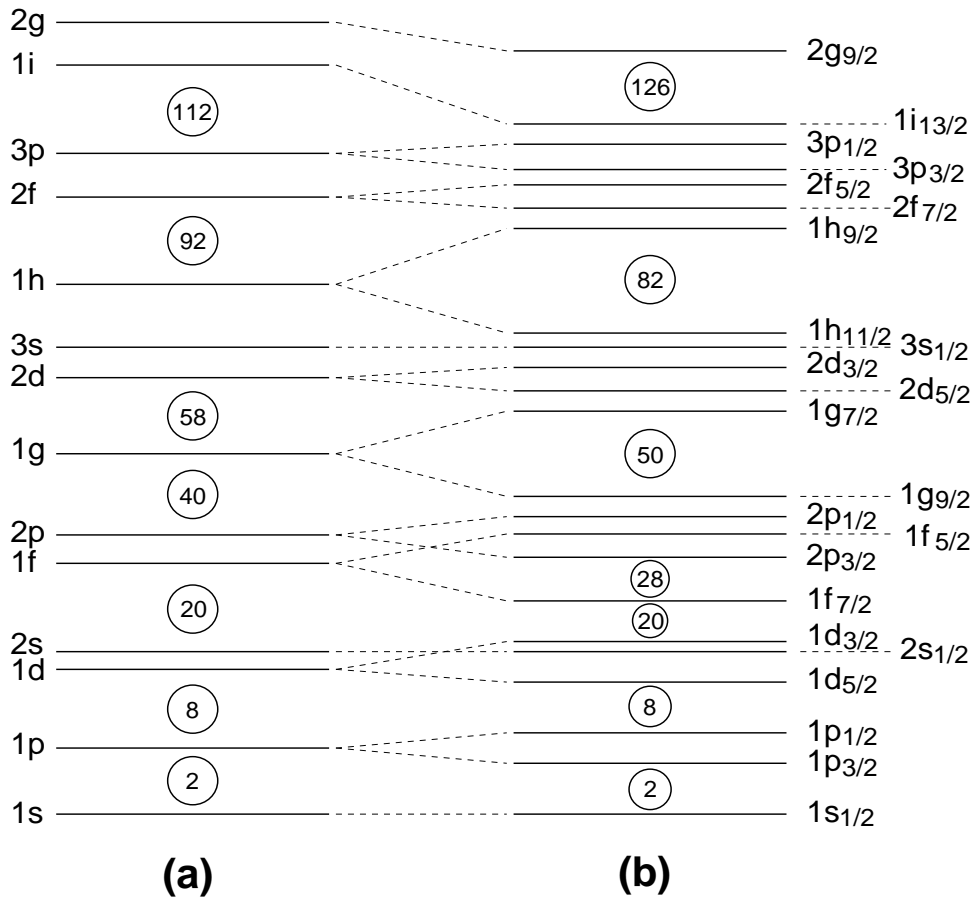


Figure 2.2: Panel (a) shows the single particle energies obtained from a Woods-Saxon potential, panel(b) the single particle energies obtained from a Woods-Saxon potential with the proper spin-orbit interaction added. The numbers in the circles are the magic numbers. The protons and neutrons are treated separately. For instance in the $1s_{1/2}$ orbit, two protons and two neutrons can each be placed.

degeneracies of the levels are now $(2j + 1)$ as the degeneracy in spin is lifted. From the figure it is evident that the experimental magic numbers are well reproduced by this model. The magic number 28 first appears when the spin-orbit interaction is included. Hence ^{56}Ni is the first doubly magic nucleus to be described by the inclusion of the spin-orbit force. For a more comprehensive description of nuclear models, see for instance Refs. [2, 4].

The doubly magic nucleus $^{56}_{28}\text{Ni}_{28}$ has 28 protons and 28 neutrons. It implies that all orbitals up to and including the $1f_{7/2}$ orbit are completely filled for both protons and neutrons. The protons (neutrons) couple to spin zero in the ground state, due to the so called pairing interaction. It means that the ground state of ^{56}Ni has spin parity 0^+ , alike all nuclei with even numbers of protons and neutrons. For a nucleus with a single unpaired nucleon the ground state spin and parity will be determined by the state of the odd nucleon.

To create an excited state from a closed shell nucleus as ^{56}Ni , a pair of nucleons needs to be broken and at least one of the nucleons needs to be lifted to a higher lying shell. This implies that the energy of that excited state is relatively high. On the other hand, nuclei with odd nucleons can create excited states by only re-coupling their angular momenta. Usually it correspond to excitations of low energy. The first excited state of ^{56}Ni has an energy of 2.7 MeV [5], whereas the first excited state of ^{57}Ni is at 0.77 MeV [6]. ^{57}Ni has the same configuration as ^{56}Ni , except for an additional neutron in the $2p_{3/2}$ orbit. The ground state and spin parity of ^{57}Ni is $3/2^-$ and the first excited state has spin and parity $5/2^-$ (cf. Fig. 2.2 (b)). Thus the ground state and the first excited state in ^{57}Ni is produced by the odd nucleon. To continue predicting excited states in this fashion soon proves very difficult. When the number of nucleons, which participate in the formation of an excited state increases, the different possibilities and ways of creating the excited state also increases. A very powerful tool in predicting excited states in nuclei are shell model calculations. In the nuclear structure group at Lund University the code ANTOINE [7, 8] is often used.

2.1.1 A shell model calculation code - ANTOINE

A shell-model calculation can be performed to compare experimental results to theoretical predictions. The shell-model calculation can among other things derive level energies, wave functions, the occupation numbers, electromagnetic moments, and transition probabilities.

The Hamiltonian used in shell model calculations describes the nucleons in a mean potential interacting through residual interactions. For two states it can be expressed as

$$H = \begin{pmatrix} \varepsilon_{a_1} & 0 \\ 0 & \varepsilon_{a_2} \end{pmatrix} + \begin{pmatrix} \langle \phi_1 | V_{11} | \phi_1 \rangle & \langle \phi_1 | V_{12} | \phi_2 \rangle \\ \langle \phi_2 | V_{21} | \phi_1 \rangle & \langle \phi_2 | V_{22} | \phi_2 \rangle \end{pmatrix} \quad (2.2)$$

where $|\phi_1\rangle$ ($|\phi_2\rangle$) are basis states. Basis states have a given spin, parity, and iso-spin, and allow the Hamiltonian to be represented (as above) with a matrix. The first matrix contains the single-particle energies. The elements in the second matrix are called two-body matrix elements. The diagonal elements represents the expectation value of V_{11} respectively V_{22} on $|\phi_1\rangle$ and $|\phi_2\rangle$. The off-diagonal elements represent configuration mixing, i.e. the effect of state 1 on state 2 and vice versa. By diagonalising the Hamiltonian matrix the energy eigenvalues for different states can be obtained. The single particle energies and the two body matrix elements form an interaction (see Sec. 2.1.2), which tries to describe an interaction as realistic as possible.

To solve the Schrödinger equation includes, as mentioned above, diagonalisation of the Hamiltonian matrix. The dimensions of the Hamiltonian rapidly becomes very large ($\geq 10^7$). In Sec. 4.2, Fig. 4.5 an example of the dimensions of the Hamiltonian matrix is shown. This depends on the fact that the number of basis states needed to describe a given level in the nucleus rapidly increases. Consequently, it is necessary to somehow restrict the shell-model calculations.

A common first step is to limit the number of nucleons which can participate in the calculation. Typically an inert core is defined, and from it no nucleons are assumed to partake in the creation of excited levels. For nuclei in the fp shell, the doubly magic nucleus ${}^{40}_{20}\text{Ca}$ is often used as an inert core. Relative to it, ${}^{56}_{28}\text{Ni}_{28}$ has eight more protons and neutrons, which are called valence nucleons.

Secondly, the number of available orbitals which nucleons can be excited into is limited. Typically, excitations from $1f_{7/2}$ into the $2p_{3/2}$, $1f_{5/2}$ and $2p_{1/2}$ orbitals are allowed.

It is also possible to restrict the *maximum* number of possible excitations, t , from the $1f_{7/2}$ orbit, i.e., the maximum number of nucleons, which can be excited into the other fp orbitals. The *absolute* number, t' , of allowed particle-hole excitations can also be determined. This enables the study of pure particle-hole excitations.

In Sec. 4.2 the results from several large scale shell-model calculations are presented.

2.1.2 Interactions

With the code ANTOINE it is possible to use different interactions. The calculations presented in Sec. 4.2 utilises two different standard interactions for the fp shell, namely KB3G [9] and GXPF1 [10, 11], both containing the $1f_{7/2}$, $2p_{3/2}$, $1f_{5/2}$ and $2p_{1/2}$ orbitals.

KB3G

The KB3G [9] interaction was developed by A. Poves *et al.* in 2001. It is a modification of the KB3 interaction, which was derived from the bare nucleon-nucleon interaction. The modifications involve changing the single-particle energies and introducing a mass dependence in the interaction, to better reproduce the shell gap at $N = Z = 28$. The interaction is derived using ${}^{40}\text{Ca}$ as a core and the single-particle energies are given by the experimental spectrum of ${}^{41}\text{Ca}$. Typically KB3G is used for nuclei situated in the lower fp shell with $A \sim 50$.

GXPF1

The GXPF1 [10, 11] interaction was developed by M. Honma *et al.* in 2002. The GXPF1 interaction is also derived from the nucleon-nucleon interaction, with 195 two-body matrix elements, and four single particle energies. These were determined by fitting the energy eigenvalues obtained from the theoretical Hamiltonian matrix to 699 experimental binding energies and energy levels in 87 nuclei in the $A \sim 60$ region, one of which was ${}^{56}\text{Ni}$. The single-particle energies were used as a parameter in the interaction, and fitted to experimental data. There is also a mass dependence in the interaction. The GXPF1 interaction is hence a more empirical interaction than KB3G.

A modification of GXPF1 called GXPF1a was presented in 2005. It was created due to the problems GXPF1 had in describing some neutron rich nuclei in the fp shell [12]. In it the single-particle energies and the two-body matrix elements have been slightly adjusted with respect to GXPF1.

2.1.3 The Coulomb energy

The Coulomb force is present in the nucleus, as the protons are positively charged. In the KB3G and GXPF1 interactions the Coulomb force is not considered. It is motivated by the fact that the strong force is approximately a hundred times stronger than the Coulomb force. Thus the Coulomb force can be seen as a small perturbation in the nucleus.

The Coulomb force is usually divided into monopole and multipole components when discussed in relation to shell model calculations. The monopole component consists of a radial- and an electromagnetic spin-orbit component. The multipole component represents the effect of breaking and aligning pairs of protons. These effects are discussed in detail in Ref. [13] and in Ref. [14]. It is possible to include the Coulomb force in the interactions by modifying the single-particle energies and the two-body matrix elements. The effect of including it for the present calculations is discussed in Sec. 4.2.4.

2.2 Electromagnetic Transitions

An excited nuclear state can decrease its energy by emitting a γ ray. It then proceeds from an initial state ψ_i to a final state ψ_f . The character of the γ ray, which can be either electric or magnetic, is denoted σ and the multipole order of the transition is denoted L . A γ ray emitted from a nucleus has a definite energy, E_γ , and angular momentum $L\hbar$. Given an excited state of the nucleus with angular momentum, \vec{J}_i , and a final state with angular momentum, \vec{J}_f , the conservation of angular momentum gives

$$\vec{J}_i = \vec{J}_f + \vec{L}$$

The angular momentum selection rules are given by

$$|J_i - J_f| \leq L \leq J_i + J_f$$

An exception to the above selection rule occurs if $J_i = J_f = 0$, as $L = 0$ γ -ray transitions are forbidden, since a photon has an intrinsic angular momentum of $1\hbar$. Thus for nuclei, transitions from $0^\pi \rightarrow 0^\pi$ are forbidden to γ decay. Typically these transitions instead decay by internal conversion.

The character of the γ -ray is determined by

$$\begin{aligned} \text{parity conserving : } & L \text{ even} \rightarrow \text{electric, } L \text{ odd} \rightarrow \text{magnetic} \\ \text{parity changing : } & L \text{ odd} \rightarrow \text{electric, } L \text{ even} \rightarrow \text{magnetic} \end{aligned} \quad (2.3)$$

A given transition can consist of several components, for instance a $4^+ \rightarrow 2^+$ transition is composed of $E2$, $M3$, $E4$, $M5$ and $E6$ components, where the $E2$ component usually is by far the strongest (see Sec. 2.2.1).

2.2.1 Transition probability

The transition probability, $\lambda(\sigma L)$, for a γ -ray emission of multipolarity L and character σ is given by

$$\lambda(\sigma L, J_i \rightarrow J_f) = \frac{8\pi(L+1)}{\hbar L[(2L+1)!!]^2} \left(\frac{E_\gamma}{\hbar c}\right)^{2L+1} B(\sigma L, J_i \rightarrow J_f), \quad (2.4)$$

where $B(\sigma L)$ is the so called reduced transition probability and E_γ is the γ -ray energy. The reduced transition probability can be expressed with the help of the reduced matrix element $\langle \psi_f || M(\sigma L) || \psi_i \rangle$

$$B(\sigma L, J_i \rightarrow J_f) = \frac{1}{2J_i + 1} |\langle \psi_f || M(\sigma L) || \psi_i \rangle|^2, \quad (2.5)$$

The electric (EL) and magnetic operators (ML) for a nucleus with A nucleons are sums over the single-particle operators

$$M(EL) = \sum_{i=1}^A e_i r_i^L Y_{Lm_L}, \quad (2.6)$$

$$M(ML) = \sum_{i=1}^A \mu_n \left(\frac{2}{L+1} g_l^i l_i + g_s^i s_i \right) \cdot [\nabla(r_i^L Y_{Lm_L})], \quad (2.7)$$

where Y_{Lm_L} are the spherical harmonic functions and r_i is the orbital radius for particle i . These operators are derived for a particle with charge e_i and magnetic moments are determined by the gyromagnetic factors g_l and g_s . If the transition is of single particle character, the reduced transition probabilities can be estimated by

$$\lambda(EL) = \frac{8\pi(L+1)}{L[(2L+1)!!]^2} \frac{e^2}{4\pi\epsilon_0\hbar c} \left(\frac{E}{\hbar c}\right)^{2L+1} \left(\frac{3}{L+3}\right)^2 cR^{2L} \quad (2.8)$$

$$\lambda(ML) = \frac{8\pi(L+1)}{L[(2L+1)!!]^2} \frac{e^2}{4\pi\epsilon_0\hbar c} \left(\frac{E}{\hbar c}\right)^{2L+1} \left(\mu_p - \frac{1}{L+1}\right)^2 \cdot \left(\frac{\hbar}{m_p c}\right)^2 \left(\frac{3}{L+2}\right)^2 cR^{2L} \quad (2.9)$$

These are the so-called Weisskopf estimates [4]. They can be compared to experimental data, and give a hint if a certain transition is of single-particle character or if it is collective.

That the lowest possible multipole order dominates for a given transition can be shown by calculating the respective transition probabilities for an $A = 56$ nucleus and a 2 MeV γ ray

$$\lambda(M1) : \lambda(E2) : \lambda(M3) = 1.0 : 4.5 \cdot 10^{-3} : 3.9 \cdot 10^{-9}$$

and

$$\lambda(E1) : \lambda(M2) : \lambda(E3) = 1.0 : 1.4 \cdot 10^{-6} : 1.2 \cdot 10^{-9}$$

From these it can also be concluded that for a given multipole order the electric radiation is more probable than magnetic radiation. It is also possible to have a

mixing of the two lowest multipole orders, for instance a $E2/M1$ mixture. The reduced transition probabilities for the former can be expressed as

$$\begin{aligned} B(M1; J_i \rightarrow J_f) &= \frac{1}{2J_i+1} |\langle J_f || M1 || J_i \rangle|^2 \\ B(E2; J_i \rightarrow J_f) &= \frac{1}{2J_i+1} |\langle J_f || E2 || J_i \rangle|^2, \end{aligned} \quad (2.10)$$

where the respective transition operators are given by

$$\begin{aligned} M1 &= \mu_N \sum_{i=1}^A [\widehat{g}_s(i) \vec{s}_i + \widehat{g}_l(i) \vec{l}_i] Y_{10} \\ E2 &= \sum_{i=1}^A \widehat{e}(i) r_i^2 Y_{20}. \end{aligned} \quad (2.11)$$

In these equations the effective \widehat{g} factors and effective charges (\widehat{e}) are used. The bare g factors for protons (neutrons) are $g_l = 1(0)$ and $g_s = 5.586(-3.826)$. However, inside the nucleus the g factors and charges for protons and neutrons might be different than for free nucleons. For instance, a valence proton can polarise the otherwise inert core. Thus effective \widehat{g} factors and effective charges are introduced. In Ref. [15] the effective charges were determined to be $\widehat{e}_p = 1.15e$ and $\widehat{e}_n = 0.8e$ for protons respective neutrons.

2.2.2 Branching ratios

If several final states can be reached in the process of the γ decay, the transition probability will be affected. The total transition probability is the sum of the individual transition probabilities. The contribution of each transition to the total decay probability, is determined by so called branching ratios, b_r . For instance, in

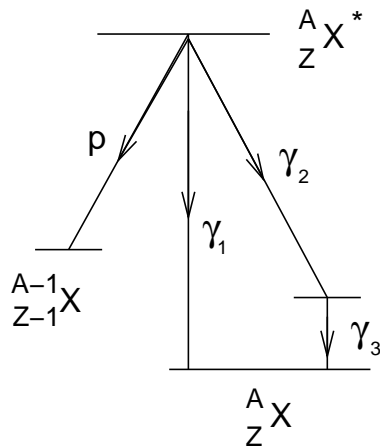


Figure 2.3: The decay of an excited state into several final states affects the branching ratios of the individual decay possibilities.

Fig. 2.3 the decay of an excited level in the nucleus $\frac{A}{Z}X$ is shown. The excited level can decay with two different γ rays and with a proton decay. The branching ratio for γ_1 will hence be

$$b_{r\gamma_1} = \frac{\lambda_{\gamma_1}}{\lambda_{\gamma_1} + \lambda_{\gamma_2} + \lambda_p}. \quad (2.12)$$

This is proportional to the experimental measured intensity

$$b_{r\gamma_1} \propto \frac{I_{\gamma_1}}{I_{\gamma_1} + I_{\gamma_2} + I_p}. \quad (2.13)$$

2.2.3 Mixing ratio

By using the transition probabilities it is possible to determine the mixing degree of a given γ -ray transition. The mixing ratio is defined as

$$\delta(\sigma_2 L_2 / \sigma_1 L_1) = \sqrt{\frac{\lambda(\sigma_2 L_2)}{\lambda(\sigma_1 L_1)}}. \quad (2.14)$$

If $\lambda(\sigma_2 L_2) = 0$ then $\delta(\sigma_2 L_2 / \sigma_1 L_1) = 0$, and the transition is said to be pure since the mixing is zero. If $L = \Delta J$ as well, the transition is said to be stretched.

2.3 Prompt particle decay

A new fascinating decay mode was discovered in ^{58}Cu in 1998 [16]. ^{58}Cu was produced through a fusion-evaporation reaction in an excited, highly deformed state. The rotational band γ decayed until the band head. Instead of the expected γ -decay out into the spherical states, a proton was emitted. The new decay mode is called ‘prompt proton decay’, because the formation of the residual nucleus, the γ -decay of the rotational band in the second minimum, the particle emission, and finally the γ decay in the daughter nucleus are observed in ‘prompt’ coincidence in thin-target in-beam fusion-evaporation experiments. Through the emission of the proton the

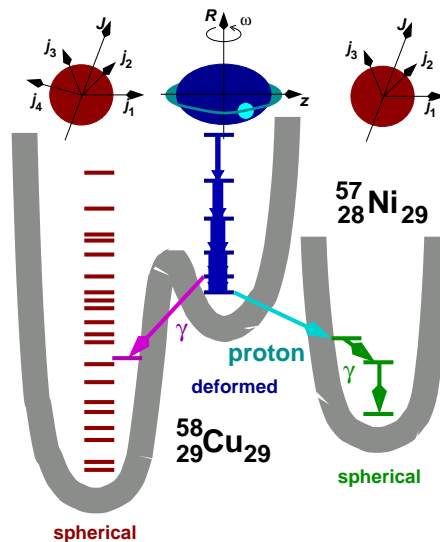


Figure 2.4: In the prompt proton decay the mother nucleus drastically changes its shape from deformed to spherical when it emits a proton. The prompt proton decay was first observed in ^{58}Cu . Picture taken from Ref. [17]

daughter nucleus ^{57}Ni is created, in a near spherical state, i.e. a drastic rearrangement of the nuclear mean field occurs during the decay. Since this first observation it has been discovered in many other nuclei in the $A \sim 60$ region, to mention a few ^{58}Ni , ^{57}Ni and ^{59}Cu . Two cases of prompt α decay have also been observed in ^{58}Ni . Hence, the decay was renamed to the 'prompt particle decay'. The prompt proton decay is schematically shown in Fig. 2.4.

The prompt proton decay is different from previously observed proton decays in some very important aspects. Firstly the prompt proton decay competes with ordinary γ radiation, whereas observed ground state or isomeric proton radioactivity competes with β^+ decay. Hence the time scale of the prompt proton decay is the same as that of the γ decay i.e. 10^{-12} - 10^{-9} s. Secondly a dramatic change of nuclear shape from the mother nucleus to the daughter nucleus occurs in the process of the decay.

The prompt particle has to tunnel through the nuclear potential to escape the mother nucleus. If the angular momentum of the mother and daughter nuclei are known then the angular momentum of the particle is also known. The measured angular distribution of the particle can be compared to the expected angular distribution. It has been suggested that if there is a difference between the expected and measured distributions that it could be related to the time it takes for the proton to penetrate the potential barrier, i.e. the tunnelling *time*. Since, if the nucleus is deformed when the proton escapes it, the proton will have a different angular distribution than if the nucleus is spherical when it is emitted. It has also been suggested that the angular distribution of prompt protons could reveal information about single particle orbitals inside deformed potentials allowing nuclear densities to be determined [18].

The main purpose of experiment 3 (c.f. Sec. 3.3) was to study the angular distributions of prompt protons. To measure with high accuracy the angular distributions a detector with a high angular coverage and granularity is needed. The Lund university Silicon Array -LuSiA- was created to meet these requirements. LuSiA is described in detail in Sec. 5. The angular distribution of prompt protons may give insights in to quantum mechanical tunnelling, a widespread phenomena not only in nuclear physics, but in the natural sciences in general.

Chapter 3

Experimental technique

The doubly magic nucleus ${}^{56}_{28}\text{Ni}_{28}$ is an unstable nucleus, which is not found naturally on earth. The lightest stable isotope of nickel is ${}^{58}\text{Ni}$. It means that ${}^{56}\text{Ni}$ is two neutrons away from stability. Hence if one wishes to study this doubly magic nucleus and other exotic nuclei, they have to be produced in a laboratory. A common experimental method to produce neutron deficient nuclei is by initiating heavy ion fusion-evaporation reactions. A compound nucleus is formed, it decays by evaporating particles and γ rays. By detecting the reaction products the residual nucleus can be identified. In Sec. 3.1 the experimental method is described and the experimental equipment is discussed in Secs. 3.2.1 and 3.2.2. The experiments which this work is based on are outlined in Sec. 3.3 along with the data handling.

3.1 Experimental method

The fusion-evaporation reaction may be thought of as a two step process. The incident beam nuclei hit the target nuclei. The individual nucleons of the beam and the target come into each others range of strong interaction, and the energy of the beam nuclei spreads throughout the whole system. The energy becomes shared between the nucleons, and a fused system is formed. The compound nucleus is excited but the average energy of the nucleons is not large enough to free it from the nucleus. But through collisions between the nucleons some of them may gain enough energy to escape the compound nucleus. The compound nucleus is thus an intermediate state existing after fusion but before decaying through particle evaporation. The compound nucleus has an excitation energy of

$$E^* = Q + E_{CM} = Q + E_b \frac{M_t}{M_b + M_t} \quad (3.1)$$

where Q is the Q value of the reaction and E_{CM} is the center of mass energy available for excitation, E_b is the beam energy and M_t (M_b) is the mass of the target (beam). The maximum angular momentum transferred to the compound nucleus is

$$L_{max} = \frac{M_t}{M_b + M_t} \cdot b_{max} \cdot \sqrt{2M_b(T_b - E_C)} \quad (3.2)$$

The maximum impact parameter which generates such a reaction is b_{max} . It can be estimated by

$$b_{max} = R_b + R_t = R_0(A_b^{1/3} + A_t^{1/3}) \quad (3.3)$$

where R_b and A_b (R_t and A_t) are the radius and the mass number of the beam (target) nucleus. The compound nucleus thus has a range of angular momentum, depending on the impact parameter. The Coulomb barrier, E_C , has to be overcome by the two positively charged nuclei in order for them to fuse together. It implies that the center of mass energy must at least be larger than the Coulomb barrier, which can be approximated by

$$E_C = 1.44 \frac{Z_b Z_t}{R_C} \quad (3.4)$$

where Z_b and Z_t are the proton numbers for the beam and the target. The largest impact parameter is expected when the Coulomb barrier is the greatest, hence it can be approximated that $R_C = b_{max}$.

The compound nucleus 'forgets' the process of formation and decays by statistical rules [4]. Many different residual nuclei can be produced from the same compound nucleus. For instance $^{56}_{28}\text{Ni}$ is produced by evaporation of 2α and $^{55}_{28}\text{Ni}$ by evaporation of $2\alpha 1n$ from the compound nucleus $^{64}_{32}\text{Ge}$. The decay probabilities depend only on the energy given to the system. The particle decay occurs within a time frame of $\leq 10^{-19}$ seconds. Particle evaporation is an effective way of reducing the excitation

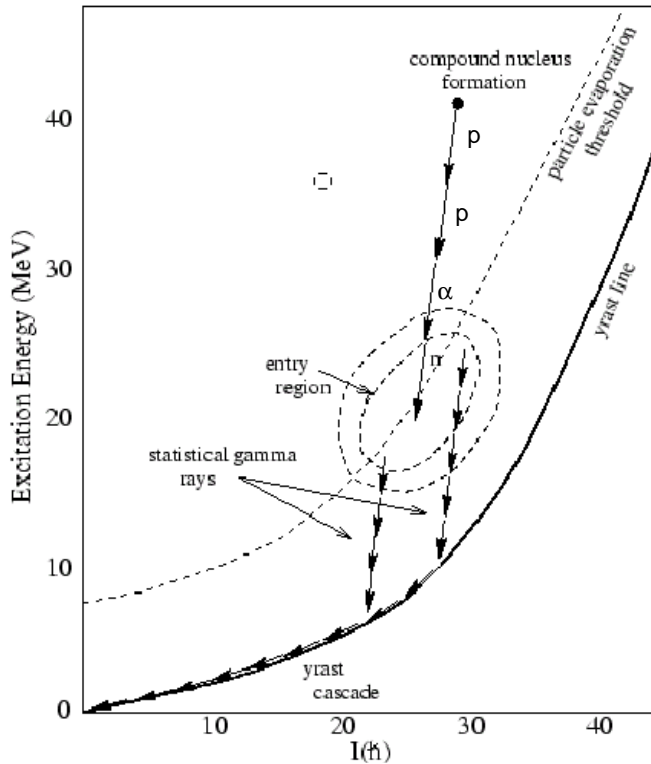


Figure 3.1: The compound nucleus formed in the fusion-evaporation reaction decays by particle and γ -ray emission. The yrast line is defined as the line connecting the states with the lowest possible energy for a given spin.

energy in the compound nucleus. For instance, an α -particle takes on average away ~ 15 MeV and protons $\sim 5-6$ MeV. The more excited the compound nucleus is, the

more particles are emitted. For the neutron deficient $A \sim 60$ region, protons and α particles are much more likely to be evaporated than neutrons. This is due to the higher neutron separation energy (~ 15 MeV) whereas the proton separation energy is ~ 5 MeV. The number of evaporated particles and their kind defines an reaction channel, and thus also defines the residual nucleus.

The average binding energy of the nucleons is about 8 MeV [4]. When the excitation energy of the compound nucleus is below ~ 8 MeV, particle evaporation is thus no longer energetically possible. The nucleus then has to decay by emitting electromagnetic radiation, i.e., γ rays. The γ rays hold much information on the structure of the nucleus, and these are the ones of interest here. The γ -ray emission continues until the nucleus reaches its ground state. This is schematically illustrated in Fig. 3.1 along with the particle evaporation threshold and the particle evaporation. The entire reaction, from formation of the compound nucleus to the ground state of the reaction product takes about 10^{-11} - 10^{-9} seconds.

The γ rays produced in the fusion-evaporation reactions studied in this thesis were detected by a Ge-detector array; Gammasphere (Sec. 3.2.1). The evaporated charged particles were detected by Microball and/or LuSiA- the Lund university Silicon Array (Sec. 3.2.2). The evaporated neutrons were detected by the Neutron Shell and the residual nuclei were separated in the Fragment Mass Analyser and identified in the ion chamber (Sec. 3.2.2). These detectors are described in Sec. 3.2.

3.2 Experimental set-up

3.2.1 Gammasphere

To detect the γ -rays emitted from residual nuclei, a state-of-the-art Ge-detector array called Gammasphere [19] was used. Gammasphere (GS) is currently placed at Argonne National Laboratory outside Chicago, U.S.A . GS can consist of up to 110 high purity Ge-detectors packed in a 4π geometry. The detectors are placed in 17 rings at angles between 17.3° to 162.7° with respect to the beam axis. The Gammasphere can be opened in two symmetrical halves. In Fig. 3.2 one of the halves can be seen. When the two halves are closed, the fronts of the Ge-detectors are 25 cm from the target position. The photo-peak efficiency in this geometry is typically $\sim 9\%$ and the energy resolution is 2.4 keV at 1.33 MeV. Gamma rays can interact with matter in three ways; the photoelectric effect, Compton scattering and pair production. For γ -ray energies between 200 - 1200 keV, Compton-scattering is the dominating interaction mode in the Ge-detectors. If a γ ray scatters in the detector it can scatter in such a way that it escapes the detector, meaning it only will deposit part of its total energy. A γ ray for which this happens will only contribute to increase the undesirable background. To suppress this background, the Ge-detectors are surrounded by BGO detectors. If a γ ray strikes a Ge-detector and then scatters into a BGO detector, the event is vetoed; it is disregarded in the data collection. In this way the number of events in the full energy peak are considerably enhanced. The BGO detectors have a poor energy resolution, but a high efficiency due to their

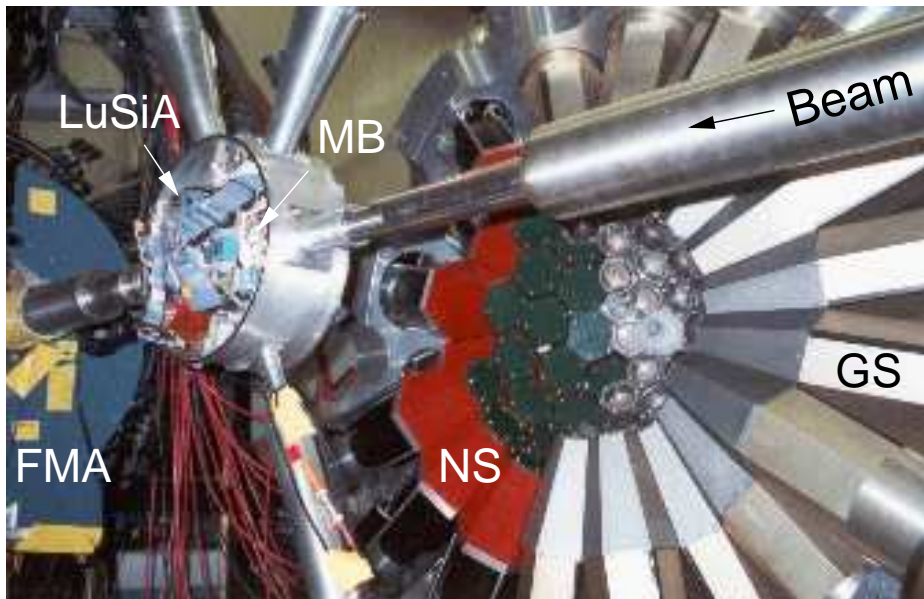


Figure 3.2: The Gammasphere (GS) is opened and one of its symmetrical halves is seen. The beam enters from the right. In the target chamber LuSiA and Microball (MB) are placed. Some of the forward detectors in GS have been replaced by the Neutron Shell (NS). To the very left in the figure, the first magnet in the Fragment Mass Analyser (FMA) can be seen.

high density and high Z . However, as the BGO detectors are primarily used as veto detectors, the poor energy resolution is not of interest, only their efficiency is important. If the γ -ray multiplicity is high, it is possible to have within the same event a γ ray impinging on a BGO detector and another one at a Ge-detector. The BGO detector will then veto a good event. To minimise this possibility heavymet absorbers can be placed in front of the BGO detectors. These can prevent the γ ray from impinging directly on the BGO detectors.

3.2.2 Ancillary detectors

In the fusion-evaporation reaction, not only γ -rays are created but also protons, α -particles, neutrons and the residual nucleus itself. To detect these various detectors are used. The Microball and LuSiA detect charged particles, the Neutron Shell detects neutrons. The residual nuclei are separated from each other in the FMA and identified in the ion chamber. The different detectors are presented below.

The Microball and LuSiA

Microball (MB) [20] and LuSiA are charged particle detectors. They are both placed in the target chamber, inside of Gammasphere (see Fig. 3.2). Microball is a scintillator detector consisting of up to 95 closely packed CsI(Tl) elements covering a maximum of 97% of solid angle. The elements are placed in 9 rings covering angles

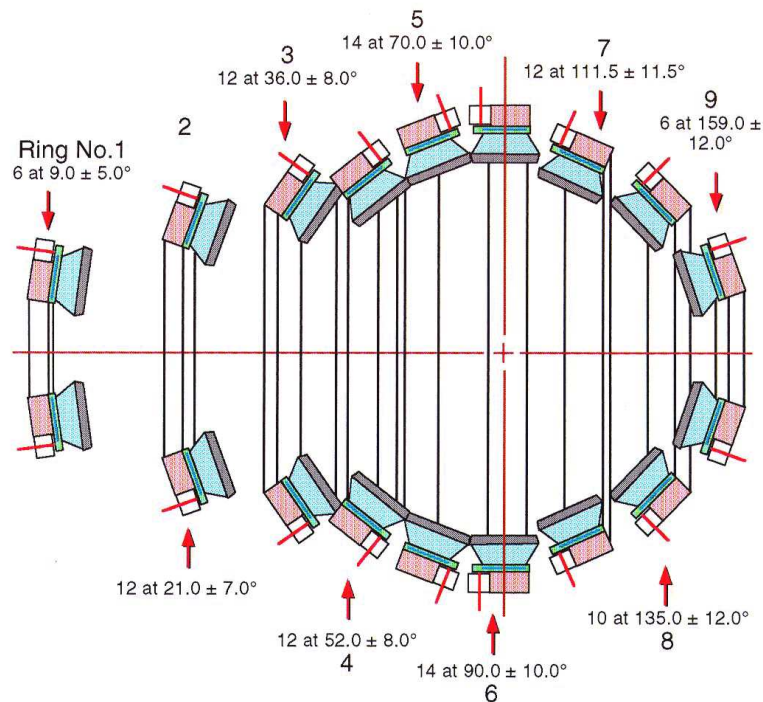


Figure 3.3: The Microball detector consists of 95 CsI(Tl) scintillator elements, placed in nine rings. Picture taken from Ref. [21].

from 4° to 171° with respect to the beam axis. These are seen in Fig. 3.3. The reaction kinematics produces particles which are strongly focused at forward angles. Therefore the most forward rings of MB are placed at a greater distance from the target. This minimises the count rates for each element, as they have a smaller solid angle, when placed further out. The distance from the target to the elements varies from 110 mm for the most forward ring to 45 mm for the most backward ring. The energy resolution of MB is 240 keV for an α particle of 8.78 MeV. Each element is covered by absorber foils consisting of either Pb or Ta to stop heavy high energy particles, i.e. scattered beam particles.

LuSiA is an array consisting of eight ΔE - E strip telescopes which together provides 2048 pixels in a near 3π geometry. The ΔE and E detectors are silicon semiconductor detectors. LuSiA is described in detail in Sec. 5.

The Neutron Shell

The Neutron Shell [22], also seen in Fig. 3.2, consists of up to 30 hexagonal liquid scintillator detectors. The four most forward rings of Gammasphere can be replaced by the Neutron Shell, which then covers $\sim 25\%$ of the solid angle. Neutron detectors can detect both neutrons and γ rays, but the detectors are covered by Pb absorbers to prevent low energy γ rays from striking the detectors. The low energy γ rays are harder to discriminate from neutrons than high energy γ rays. Alike γ rays, neutrons are more difficult to detect than charged particles. This is mainly due to the different interaction mechanisms involved when these particles interact with matter. Charged particles lose energy continuously when passing through matter

due to electromagnetic interaction with mainly the electrons in the detector. Neutrons are electrically neutral, thus they can only interact by nuclear scattering in the detector. When the neutron scatters on a nucleus in the detector, it gives rise to a small recoil. The recoiling nucleus will electromagnetically interact with the rest of the detector material, this energy can be measured. To optimize the neutron interaction, hydrogen rich material is often used as a detector material and the volume of these is typically large.

The Fragment Mass Analyser and Ion Chamber

The Fragment Mass Analyser (FMA) is a recoil mass spectrometer located at the ATLAS accelerator at Argonne National Laboratory in the U.S.A. It is used to sepa-

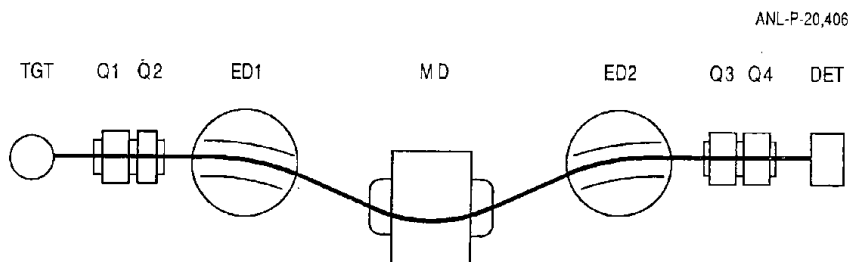


Figure 3.4: The FMA consists of dipole and quadrupole magnets (MD, Q) and dipole electric (DE) fields to separate residual nuclei from each other and from beam primary ions. Picture taken from Ref. [23].

rate residual nuclei from the primary heavy ion beam as well as residual nuclei from each other. The FMA is a system of magnetic and electric fields, seen in Fig. 3.4. The magnetic and electric fields of up to 500 kV across a 10 cm gap [23] are used to guide the residual nuclei and focus them onto the ion chamber at the end of the FMA. The ions are dispersed by mass to charge ratio (A/q) at the focal plane at the very end of the FMA.

The ion chamber at the back of the FMA has an anode segmented into three parts [24]. This allows the different energy losses of the ions to be detected. The three segments are along the beam direction, it is also segmented in the perpendicular direction to allow high count rates.

3.3 The experiments and data handling

The work presented in this thesis is based on three fusion-evaporation reaction experiments; GSFMA66, GSTOT and GSFMA138. Hereafter they will be called experiment 1, 2 and 3. The details of the experiments are summarised in Tab. 3.1.

Experiment	GSFMA66 1	GSTOT 2	GSFMA138 3
Beam	^{28}Si	^{32}S	^{36}Ar
Beam energy	122 MeV	130 MeV	134 MeV
Target	$0.5 \text{ mg/cm}^2 \text{ }^{40}\text{Ca}$	$0.5 \text{ mg/cm}^2 \text{ }^{28}\text{Si}$	$0.2 \text{ mg/cm}^2 \text{ }^{28}\text{Si}$
Compound nucleus	^{68}Se	^{60}Zn	^{64}Ge
L_{max}	$47\hbar$	$41\hbar$	$43\hbar$
Channel	3α	$2p2n$	2α
Equipment:			
Gammasphere	103 detectors	78 detectors	77 detectors
Heaviemets	no	no	no
BGO	—	—	yes
Microball	95 elements	95 elements	16 elements
LuSiA	—	—	2048 pixels
Neutron Shell	—	30 detectors	30 detectors
FMA	—	—	yes
Ion chamber	—	—	yes

Table 3.1: Details of the fusion-evaporation experiments which the present work is based on.

The analysis procedure, results and interpretation of experiment 1 and 2 are discussed in Sec. 4. The analysis of these experiments started from so called E_γ - E_γ matrices (c.f. Sec. 4.1.1). The aim of this analysis was to study the doubly magic nucleus ^{56}Ni . The experimental results from the analysis of these two experiments are shown in Sec. 4 and compared to large scale shell model calculations in Sec. 4.2.

Experiment 3 is one of the most complex experiments performed with Gammasphere and the data set taken is one of the largest from a fusion-evaporation reaction. The experiment was approximately two weeks long, and took place during the spring of 2004. From Tab. 3.1 it can be seen that the data signals collected come from Gammasphere Ge- and BGO elements, Microball, LuSiA, the Neutron Shell, the FMA, and the Ion Chamber. About 360 Gigabytes of data was taken.

The main purpose of experiment 3 was to study the angular distribution of particles emitted in the so called prompt particle decay (c.f. 2.3) but also to study exotic neutron deficient nuclei in the $A \sim 60$ region.

The data handling of experiment 3, has been performed by three PhD students. The calibration of Gammasphere and the BGO detectors has been done by D. Torres [25]. The Neutron Shell, the FMA and IC has been handled by L-L. Andersson [26]. The author has calibrated LuSiA and Microball. At the moment of writing (November 2006) a complete code, to handle all of the signals from the detectors during the experiment is being constructed. A brief overview of the data handling performed for the different detectors is given here. For detailed descriptions the reader is referred to Refs. [25, 26] and Sec. 5.

- **The Ge-detectors**

To gain match the Ge-detectors standard γ -ray emitting sources were used; ^{152}Eu and ^{56}Co . A third order polynomial was used, to convert the measured signals into energy. Since the beam provided by the ATLAS facility at Argonne National Laboratory is pulsed with an 80 ns pulse, all of the Ge-detector time signals could be aligned to the beam pulse. Unlike the sources, the residual nuclei γ decay in flight. The emitted γ -rays are thus Doppler shifted. A second order Doppler correction term was used

$$E_{\gamma} = E_{\gamma 0} \left(1 + \beta \cos \theta + \beta^2 (\cos^2 \theta - 0.5) \right) \quad (3.5)$$

where β is v/c and θ is the angle between the γ ray and the recoil nucleus direction.

- **The BGO detectors**

The BGO detectors were also gain matched using ^{56}Co . A second order polynomial was found to give an accurate transformation from the measured values to the energy. The BGO detectors were time aligned in the same way as the Ge-detectors. This is further described in Ref. [25].

- **The Microball and LuSiA**

Both Microball and LuSiA were gain matched using an α decaying source and a beam of protons impinging on a ^{12}C target. The calibration of LuSiA is described in Sec. 5 and Microball was calibrated in a similar way. To identify the charged particles in Microball, a pulse shape technique was used. This is discussed in Ref. [26].

In LuSiA the charged particles are identified using ΔE - E matrices. In Sec. 5 an example of the separation between the protons and α -particles is given in Fig. 5.15 (a).

- **The Neutron Shell**

To separate neutron signals from γ ray signals in the neutron detectors, a pulse-shape technique was utilised. The signals taken from the neutron detectors were combined in different matrices to create an optimum separation between the neutrons and γ rays. For the neutrons an energy calibration is not performed, as it is only necessary to have a positive identification of the evaporated neutrons.

If in the same event, neutrons are detected in adjacent detectors, the event is disregarded as it is considered to be one neutron scattering from one detector to the next. This two neutron suppression is described in Ref. [26].

- **The FMA and IC**

The residual nuclei separated in the FMA are focused onto the focal plane detector at the end of it. The focal plane detector will provide a determination of the mass to charge ratio. Next the residual nucleus enters the ion chamber, where it will lose energy. Since the anode of the IC is split, the different energy loss signals, which are proportional to the number of protons in the nucleus, can be combined to obtain an optimum separation between the different nuclei. This process is further described in Ref. [26].

- **Event-by-event Doppler correction**

The compound nuclei will have a momentum vector in the beam direction due to the kinematics of the reaction. When the compound nucleus evaporates particles, a small recoil is given to the residual nucleus. By measuring the energy of the evaporated particles and the struck pixel/element reveals the angle, it is possible to reconstruct their momentum. This in turn allows for a correction to the recoil vector of the the residual nuclei. The energy of an evaporated particle in the center of mass system is given by

$$E_{cm} = E_{lab} + E_{kin} - 2\sqrt{E_{lab}E_{kin}}\cos\theta \quad (3.6)$$

where E_{kin} is the kinetic energy of particles at the time of evaporation. θ is the angle between the beam direction and the detector element/pixel. When the recoil vector of the residual nucleus is accurately known, a better resolution of the measured γ -ray peaks can be obtained. As the angle θ is the angle between the event-by-event recoil vector and the detector, rather than between the beam line and the detector. This procedure is described in Ref. [25].

To obtain with certainty the energy of the evaporated particles, both the measured energy in the detectors and the angle have to be accurately known. The method of how to obtain the energy and the angle for LuSiA is discussed in Sec. 5.

- **Sorting**

The last stage of the data handling consists of sorting the γ -rays associated with an identified residual nucleus into various one dimensional spectra and $E_\gamma - E_\gamma$ matrices. From the matrices it is possible to construct level schemes, which is described in Sec. 4.1. Finally, from these nuclear structure physics can be derived.

Chapter 4

The doubly magic nucleus ^{56}Ni

The doubly magic $N = Z = 28$ nucleus ^{56}Ni has been investigated experimentally with two fusion-evaporation reactions which are described in Sec. 3.3 and in Paper 1. The results discussed in this chapter include a significantly extended level scheme of ^{56}Ni (Sec. 4.1) which is compared to large scale shell-model calculations in the fp shell (Sec. 4.2).

4.1 Experimental results

Fusion-evaporation reactions using Gammasphere in conjunction with ancillary detectors create huge amount of data signals. A certain portion of this data is written to tape on an event-by-event basis. Typically for experiments like these ones a few billion events are written to tape, which corresponds to hundreds of Gigabytes. This huge amount of data requires careful handling to achieve the desired quantity; a specific nucleus along with its γ -rays. For more information on the data handling, the reader is referred to Refs. [27, 28]. The experimental results concerning ^{56}Ni are given in Paper 1. In Sec. 4.1.1 and Sec. 4.1.2 it is briefly described how these results were obtained.

4.1.1 Coincidence spectroscopy

To create an experimental level scheme of ^{56}Ni , $E_\gamma - E_\gamma$ correlation matrices were created. In these, it is possible to select or gate on one specific γ -ray energy on one of the E_γ axes and project it out onto the other axis. The spectrum created in this way reveals which γ rays are in coincidence with each other. In the upper part of Fig. 4.1 an example of a coincidence spectrum is shown. It is gated on the $6^+ \rightarrow 4^+ \rightarrow 2^+ \rightarrow 0^+$ yrast cascade in a 3α -gated $\gamma\gamma$ coincidence matrix, which corresponds to the residual nucleus ^{56}Ni created in experiment 1 (c.f. Sec. 3.3). All of the transitions seen in this spectrum are in coincidence with the transitions gated on. To see in more detail which γ -rays are in coincidence, a gate can be put on any of the transitions. For example, the spectrum obtained if a gate is put on the 1055 keV transition is shown in the lower part of Fig. 4.1. It displays the γ -rays in coincidence with the 1055 keV γ -ray. Taking into account the relative intensity of the transitions, it is possible to determine in which order the γ -rays are emitted. Hence by gating in $E_\gamma - E_\gamma$ matrices and measuring the intensity of the coincident

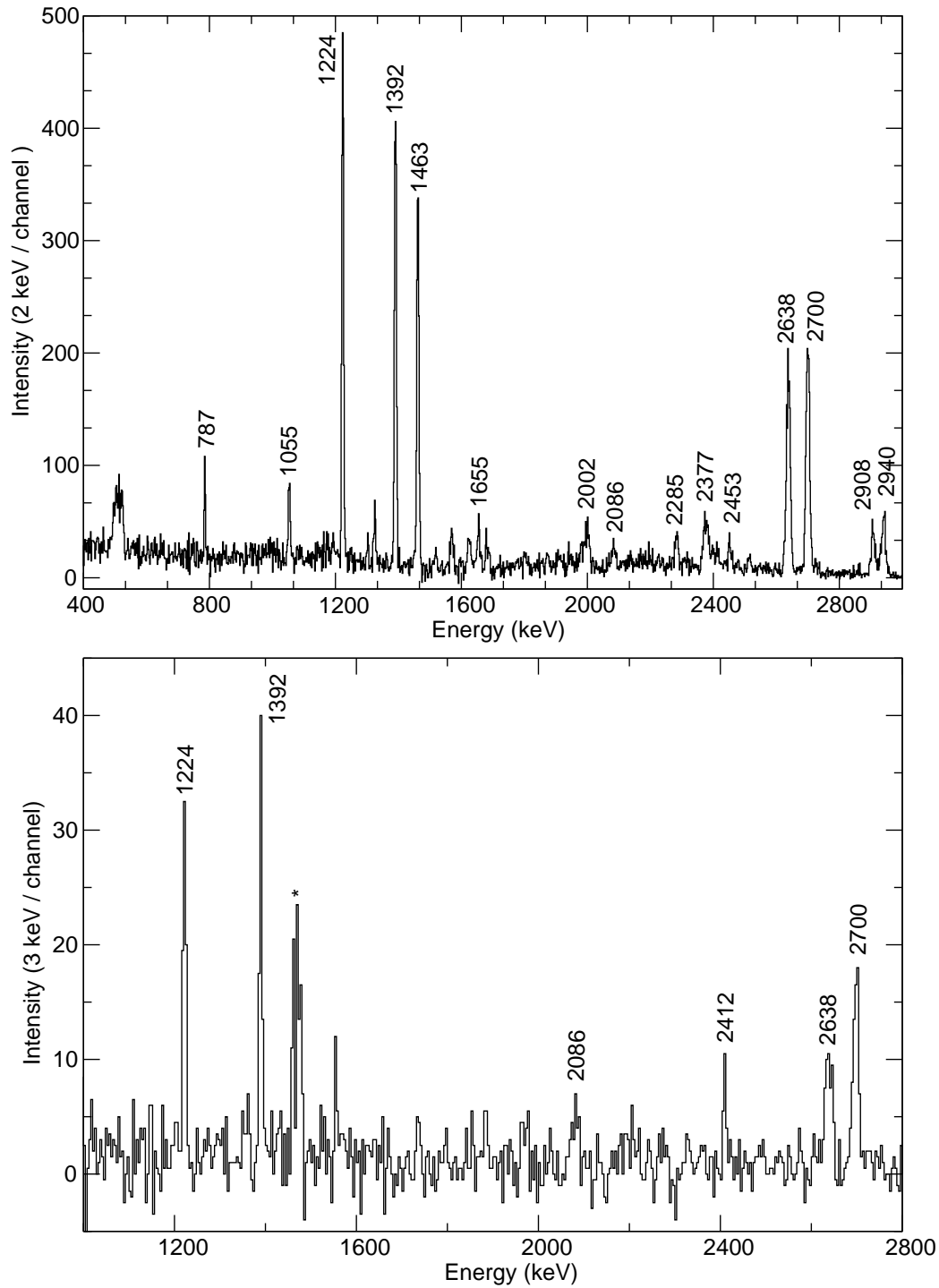


Figure 4.1: Top: The coincidence spectrum created by gating on the $6^+ \rightarrow 4^+ \rightarrow 2^+ \rightarrow 0^+$ yrast cascade in ^{56}Ni . Bottom: The coincidence spectrum for the 1055 keV transition. The peak marked with a star, is the $2^+ \rightarrow 0^+$ transition in the contaminating 2p2n channel, which corresponds to ^{58}Ni .

γ rays, it possible to construct a level scheme of the excited states in ^{56}Ni . The level scheme resulting from the present study is displayed in Fig. 4.2.

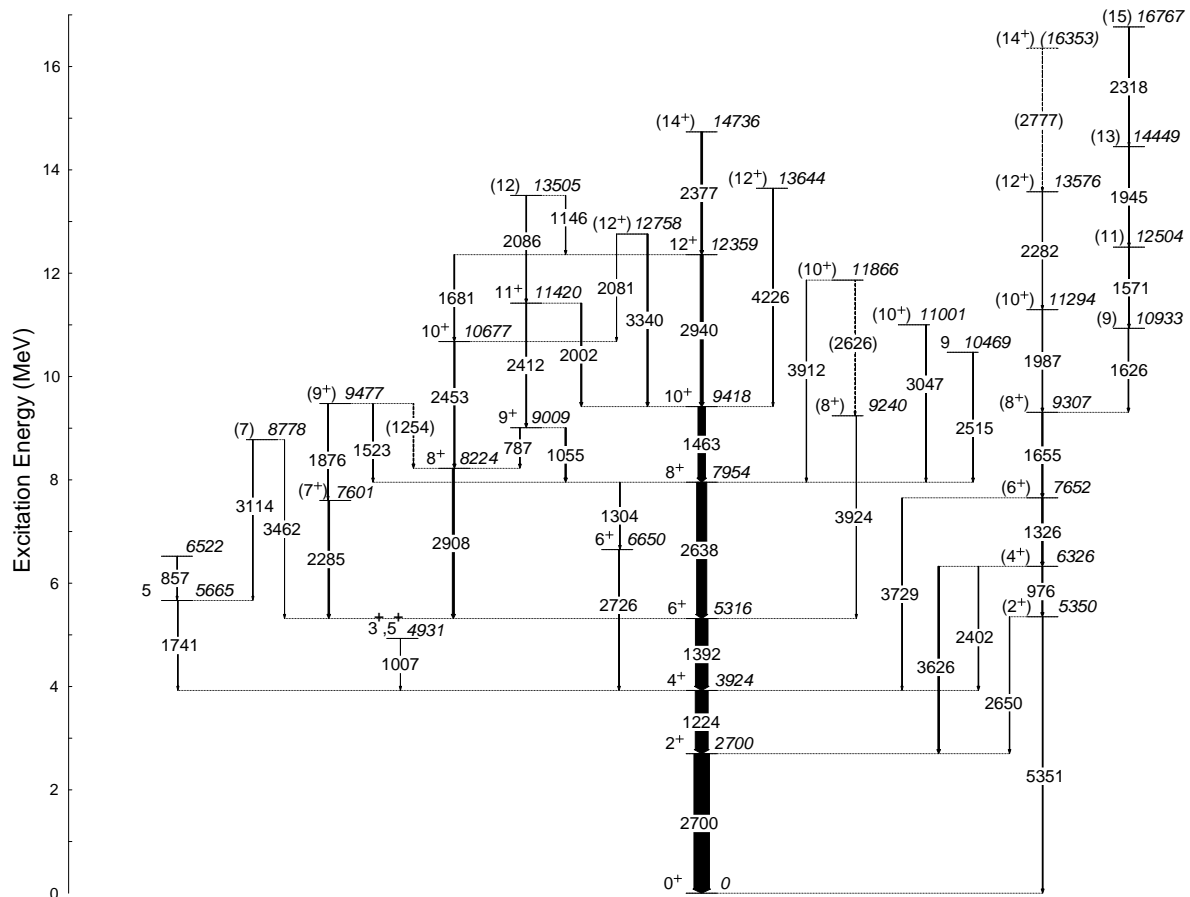


Figure 4.2: The experimental level scheme obtained from the analysis of experiments 1 and 2. In total some ~ 20 γ rays have been added to the level scheme with respect to Ref. [17]. The thicknesses of the arrows correspond to the relative intensity of the transitions, and the energies are given in keV. This is the level scheme presented in paper 1.

In Fig. 4.3 the summed intensity for all even yrast levels versus excitation energy, for experiment 1 (experiment 2) is shown in the black (red). From the figure the difference between the two experiments becomes apparent. In experiment 1 more excitation energy is present in ^{56}Ni , leading to more high-spin states. In experiment 2, ^{56}Ni is produced at a lower excitation energy, hence providing low energy states. This difference between the two experiments is also seen in Table 1 of paper 1, which shows the experimental level energies, the γ -ray transition energies, as well as the spin parity of the initial and final states. It is also what could be expected based on the L_{max} values displayed in Tab. 3.1.

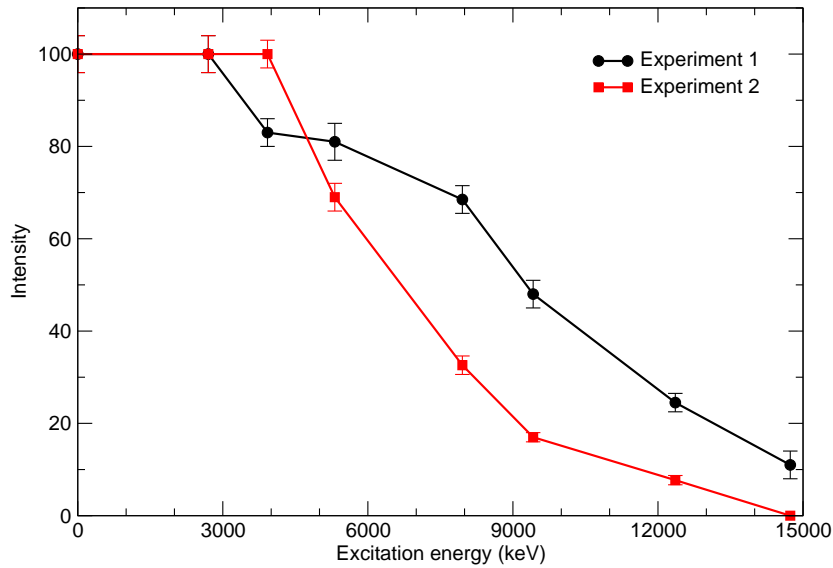


Figure 4.3: The summed intensity for all even yrast levels as a function of energy for experiment 1 (black curve) and for experiment 2 (red curve), for ^{56}Ni .

4.1.2 Spin and parity assignments

To determine the spin of the excited levels in ^{56}Ni intensity ratios were used. It reveals the relative angular momentum between two states. The ground state spin and parity of ^{56}Ni is known as 0^+ , it is thus possible to determine the spin and parity for the rest of the levels relative to the ground state with the help of $R_{30/83}$.

In fusion-evaporation reactions the compound nucleus has an angular momentum vector in a plane perpendicular to the beam axis. This so called spin alinement is slightly destroyed in the process of particle evaporation and subsequent γ -ray emission. The γ -rays emitted from a nucleus have specific angular momenta, and their angular distributions are given by the spherical harmonics. Hence the measured angular distribution at different angles relative to the beam axis allows their multipolarity to be determined.

For experiment 1 and 2, the Ge-detectors placed at 30° and 83° were used to determine the intensity ratio, $R_{30/83}$;

$$R_{30/83} = \frac{I(\gamma \ 30^\circ)}{I(\gamma \ 83^\circ)}$$

In Fig. 4.4 the angular distribution for a $\Delta I = 1$ and a $\Delta I = 2$ transition is displayed for a full spin alinement. As the spin alinement is destroyed by evaporated particles, it is expected that stretched $\Delta I = 2$ transitions have $R_{30/83} \sim 1.2$ and stretched $\Delta I = 1$ transitions have $R_{30/83} \sim 0.8$. Significant deviations from these values can be an indication of a mixed transition. Thus by measuring the intensity for the γ -rays at different angles, the $R_{30/83}$ can be obtained, allowing the spin difference

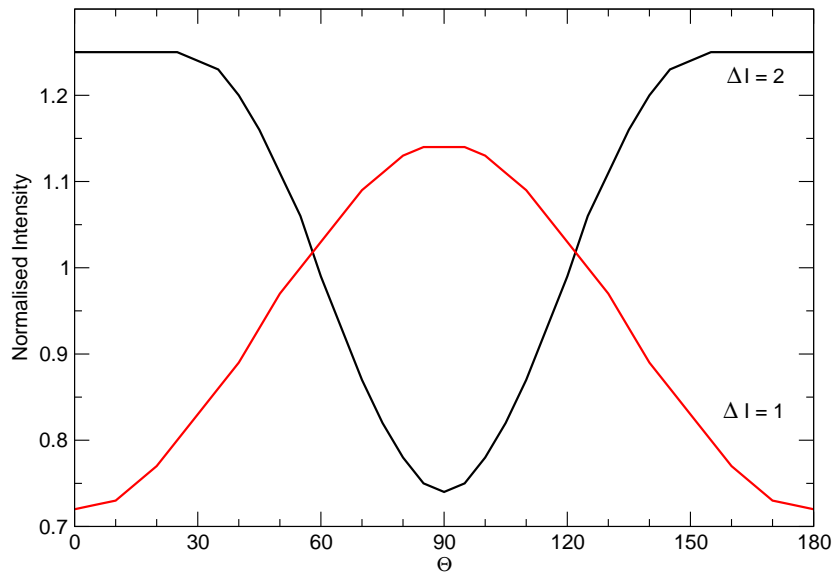


Figure 4.4: The angular distribution for a $\Delta I = 1$ and a $\Delta I = 2$ γ -ray transition, from a fully aligned residual nucleus.

between two excited states to be determined.

To deduce the parity of the nuclear states, the character of the γ -ray transitions has to be determined. Here we make use of the fact stated in Sec. 2.2.1, that transitions of electric character are much more probable than transitions with magnetic character, for a given multipolarity. If we assume that the lowest permitted multipole dominates it implies that the parity conserving $\Delta I = 2$ transitions are $E2$ transitions and that parity breaking $\Delta I = 1$ transitions are $E1$ transitions.

The spin and parity of the excited states of ^{56}Ni were determined in this fashion. The assignments are included in the experimental level scheme of ^{56}Ni , see Fig. 4.2 and in Table 1 of Paper 1.

4.2 Shell model interpretation

To compare the experimental results with theoretical results large-scale shell-model calculations were performed. The shell model code ANTOINE [7, 8] was used, with the KB3G [9] interaction and the GXPF1 [10, 11] interaction. The full fp space was utilised, including the $1f_{7/2}$ orbital below the $N = Z = 28$ shell gap and the $2p_{3/2}$, $1f_{5/2}$ and $2p_{1/2}$ above it.

In Sec. 4.2.1 the level energies for the different calculations are described, in Sec. 4.2.2 the occupation numbers are discussed and the pure particle hole excitations are presented in Sec. 4.2.3. The effect on the level energies by including the Coulomb force is considered in Sec. 4.2.4 and the transition probabilities are surveyed in Sec. 4.2.5.

4.2.1 Level energies

Figure 4.5 compares the experimental even spin yrast states up to $I^\pi = 10^+$ with the calculated level energies, for different numbers of allowed excitations, t . The interaction used to produce the level energies was either GXPF1 or KB3G without Coulomb effects included. The dimensions of the calculation dramatically increases when t increases. They are given in Fig. 4.5 and further increases to $1.1 \cdot 10^9$ for an unrestricted calculation, i.e., $t = 16$ [29]. The figure shows that the experimental level energies are best described by the $t = 6$ calculation for GXPF1 interaction. It is possible that $t > 6$ would be even better. However, it is not feasible to perform calculations with $t \geq 7$ with the computers available in the Nuclear Structure Group at Lund University. According to Ref. [9], $t = 5$ is enough to describe the most relevant states. However Ref. [29] claims that $t = 10$ is necessary to have a good reproduction of the experimental states.

The KB3G interaction cannot reproduce the experimental level energies very well even with $t = 6$. Especially noteworthy is the 2^+ state, which according to the KB3G interaction should have an energy of 4.33 MeV. The experimental energy for this level is 2.70 MeV. The poor agreement persists for the other excited states as well. From the figure it is evident that GXPF1 is quite successful in describing the experimental level energies. The largest discrepancy between the GXPF1 results and the experimental values appears for the 8^+ , 10^+ and 12^+ states, with the energy difference between the experimental and calculated 12^+ amounting to some 0.5 MeV.

The energy of the first 2^+ state in ^{56}Ni is rather low compared to other doubly magic nuclei. For instance, in $^{40}\text{Ca}_{20}$ the first excited state has an energy of 3.9 MeV. One signature of a doubly magic nucleus is a high excitation energy of the first excited state, so comparably ^{56}Ni may not be a good doubly magic nucleus.

For a comparison between non-yrast experimental and theoretical level energies calculated by GXPF1 the reader is referred to paper 1, figure 6.

In absolute values the ground state energy of ^{56}Ni calculated with GXPF1 is -206.3 MeV for $t = 6$. From the measured ground state mass, the binding energy of the ground state is calculated to -501 MeV. Hence GXPF1 can reproduce the relative level energies, it cannot reproduce the absolute values.

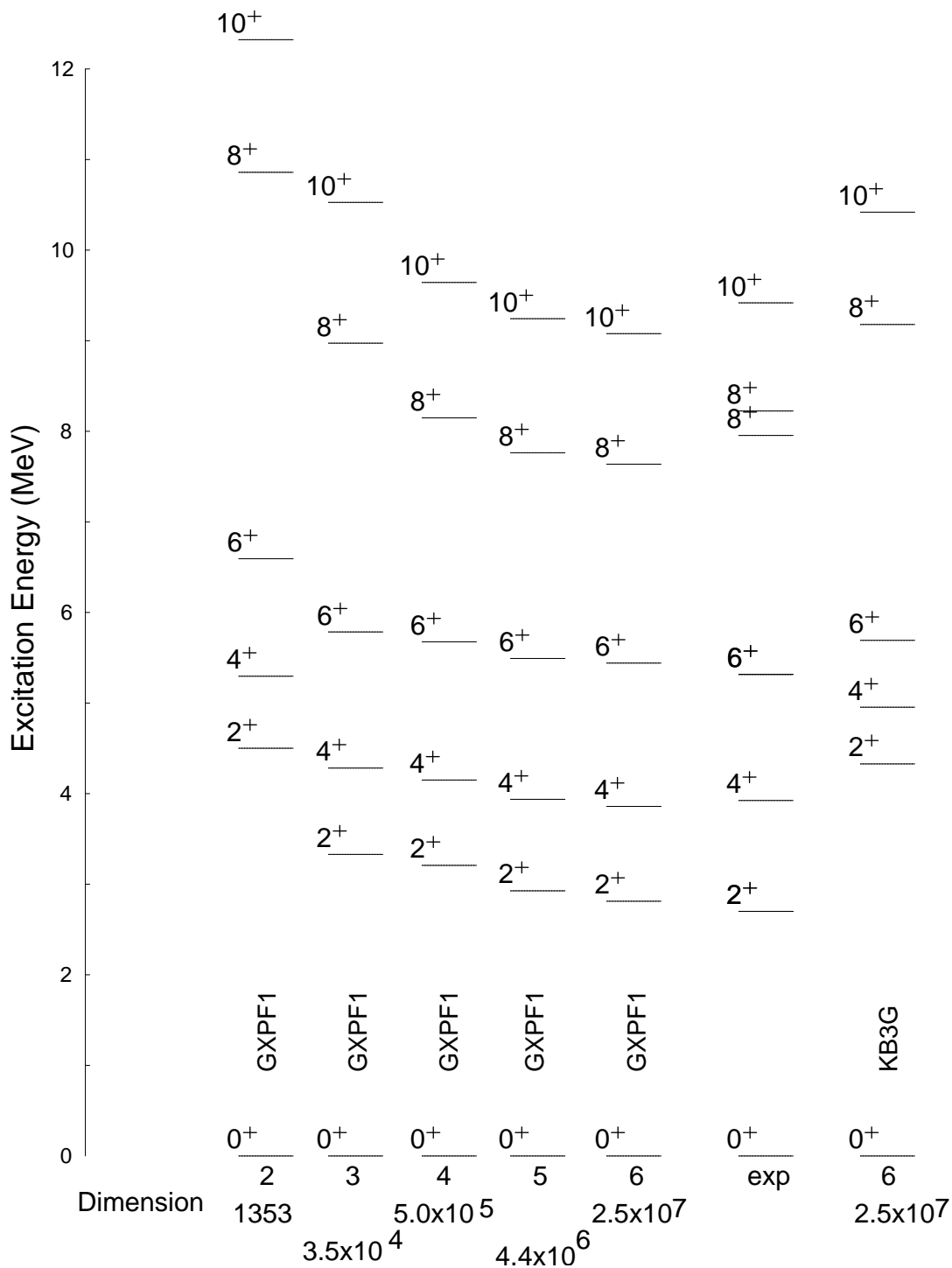


Figure 4.5: Comparison between the experimental yrast level energies and the calculated level energies for $t = 2, 3, 4, 5,$ and 6 , for even spin values up to $I^\pi = 10^+$ using GXPf1. The results for a $t = 6$ calculation using KB3G is also included. Clearly GXPf1 is better at reproducing the experimental level energies than KB3G.

4.2.2 Occupation number

Figure 4.6 displays the occupation of the fp shells as a function of spin. Once more, only the yrast states are included. It is noteworthy that the ground state of ^{56}Ni , according to the calculation, has ~ 15 nucleons in the $1f_{7/2}$ orbital. In its ground state ^{56}Ni is supposed to fill the $1f_{7/2}$ orbital completely, forming a closed proton and neutron shell. It is surprising that approximately one particle is "excited" already in the ground state. This excitation is mainly present in the $2p_{3/2}$ orbital.

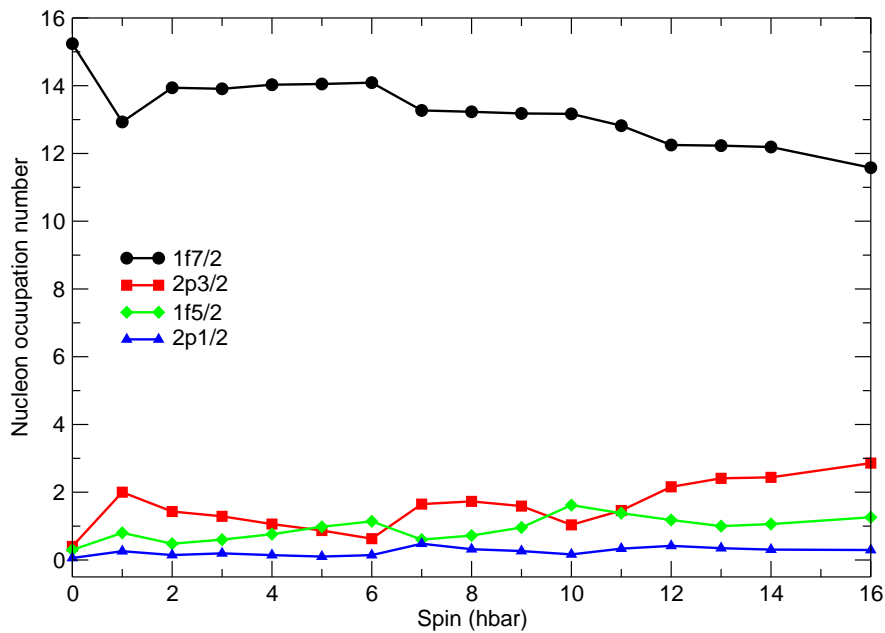


Figure 4.6: The theoretical nucleon occupation number as a function of spin for the fp orbitals, using the GXPF1 interaction, considering only the yrast spin states.

In recent articles it has been discussed if ^{56}Ni is a good doubly magic nucleus, i.e., if the $N = Z = 28$ shell gap is large enough in energy to be called a shell gap. This can be yet another indication that ^{56}Ni is not a purely closed shell nucleus even in the ground state.

The first 2^+ state, has an occupation of about 14 particles in the $1f_{7/2}$ orbital. Comparing this to the ground state, it is tempting to imagine that this excited state is created by one additional particle-hole excitation on top of the generic one-particle one-hole 'noise' level of the ground state. This particle is at first predominantly in the $2p_{3/2}$ orbital. Combining a hole in the $1f_{7/2}$ orbital with a particle in the $2p_{3/2}$ orbital, the possible excited states are 5^+ , 4^+ , 3^+ and 2^+ . Indeed, the occupation numbers are very similar for these states. However, with the above combination, it is not possible to create a 6^+ state. Here it is favourable to create the excited state with predominantly an $1f_{5/2}$ particle. The remaining yrast states seem to be created by a larger number of proton and neutron excitations.

4.2.3 Pure particle hole excitations

The energy levels obtained with t' particles excited from $1f_{7/2}$ to the upper fp shell are displayed in Fig. 4.7. The calculated energy levels for $t = 6$ using GXPF1 is included as a reference as well as some experimental levels. The experimental level energies are shifted so that the calculated and experimental 2^+ levels have the same energy.

The $t' = 1$ spectrum is very similar to the $t = 6$ spectrum, if the difference in ground state energies is neglected. It is also very similar to the experimental yrast $6^+ \rightarrow 4^+ \rightarrow 2^+$ cascade. This implies that the first three excited yrast states are build up by one-particle one-hole excitations, in agreement with the argument in Sec. 4.2.2.

The $t'=2$ spectrum has a vibrational character. This is indicated by the nearly constant energy difference between the first 0^+ , 2^+ and the 4^+ states. However, there are no experimental levels corresponding to these theoretical vibrational states in the present analysis.

The energy of the first four levels calculated using $t' = 4$ are 0, 0.567, 1.670, and 3.113 MeV. The energy for a rotating quantum object is

$$E = \frac{\hbar^2}{2\xi} I(I + 1)$$

where ξ is the moment of inertia and I is the angular momentum. When the angular momentum of the nucleus increases the rotational energy also increases. The energy levels are said to form a rotational band. Assuming that the first four states calculated by $t'=4$ form a rotational band, the factor $(\frac{\hbar^2}{2\xi})$ can be calculated through

$$\begin{aligned} E(0^+) &= 0 \\ E(2^+) &= 6 \cdot \left(\frac{\hbar^2}{2\xi}\right) = 0.567 \text{ MeV} \\ E(4^+) &= 20 \cdot \left(\frac{\hbar^2}{2\xi}\right) = 1.67 \text{ MeV} \\ E(6^+) &= 42 \cdot \left(\frac{\hbar^2}{2\xi}\right) = 3.113 \text{ MeV} \end{aligned}$$

It is for the 2^+ , 4^+ and 6^+ states 0.095, 0.084 and 0.074 MeV. The factors are sufficiently similar to conclude that the pure 4p-4h excitations form a rotational band. For comparison, the same factor is calculated for the experimental yrare energy levels;

$$\begin{aligned} E(0_3^+) &= 0 \\ E(2_2^+) &= 6 \cdot \left(\frac{\hbar^2}{2\xi}\right) = 0.35 \text{ MeV} \\ E(4_2^+) &= 20 \cdot \left(\frac{\hbar^2}{2\xi}\right) = 1.33 \text{ MeV} \end{aligned}$$

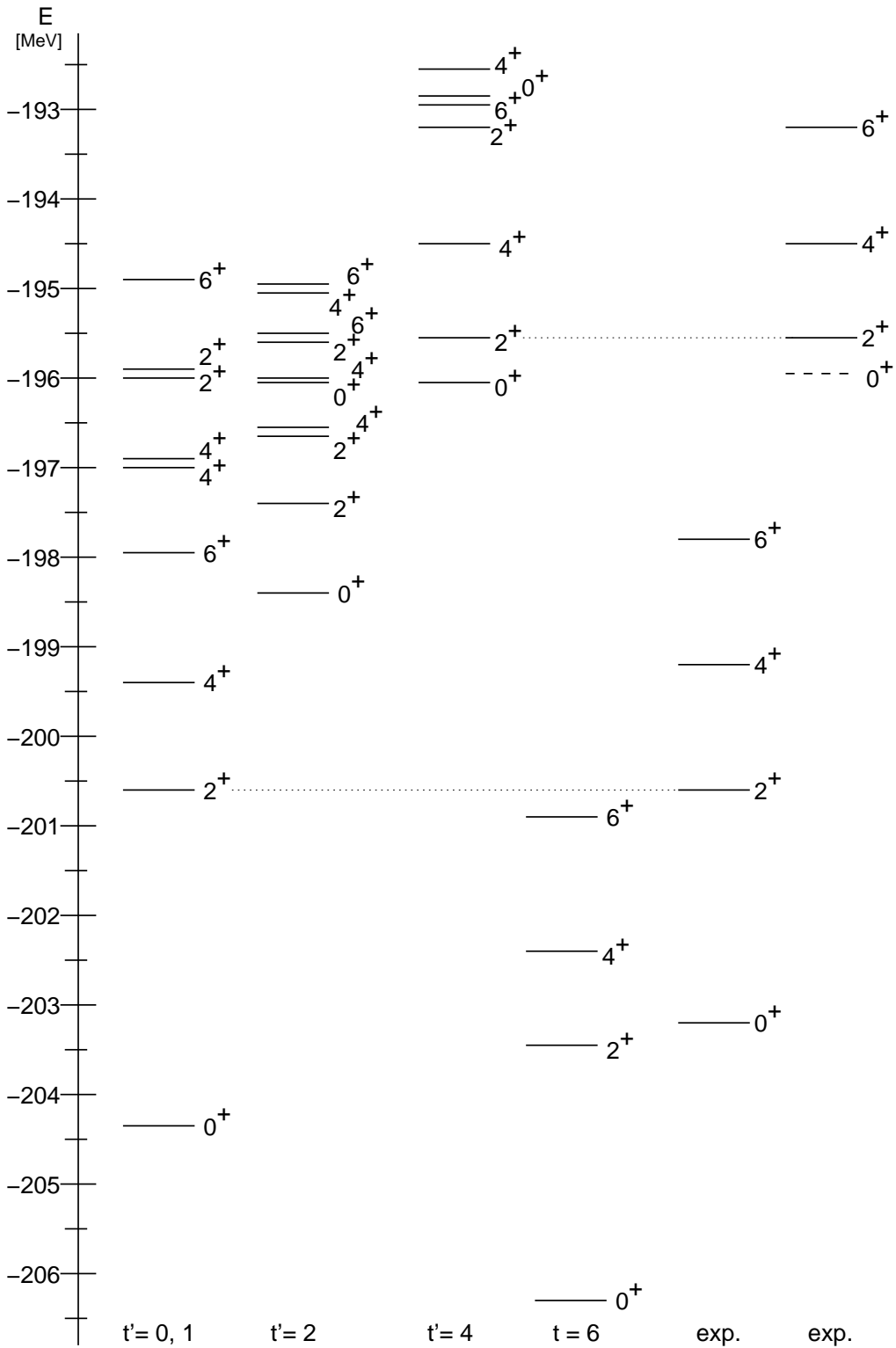


Figure 4.7: The pure $t'p-t'h$ excitation spectra, for $t' = 0, 1, 2,$ and 4 . For comparison the calculation using $t = 6$ and some experimental levels are included. The experimental level energies are shifted to concur with the calculated 2^+ energies. The dotted line corresponds to a known 0^+ state, which is not observed in these experiments. The $2p-2h$ excitations display a vibrational character and the $4p-4h$ excitations form a rotational band.

$$E(6_2^+) = 42 \cdot \left(\frac{\hbar^2}{2\xi}\right) = 2.65 \text{ MeV}$$

with the experimental energies scaled to the known 0_3^+ state with an excitation energy of 5.00 MeV. This third 0_3^+ state was not seen in the present analysis. The $\left(\frac{\hbar^2}{2\xi}\right)$ factors of 0.058, 0.067 and 0.063 MeV are obtained. Hence, it seem like the experimental states also form a rotational band.

The presence of a rotational band, implies that ^{56}Ni is deformed, as rotation in a quantum spherical object is not observable. In fact two deformed rotational bands are known in ^{56}Ni , these are shown in Paper 1.

4.2.4 Coulomb effects

The Coulomb interaction can be included in the shell model calculations by modifying the single-particle energies and two-body matrix elements. These are increased or decreased to mimic the effect of the Coulomb force in the nucleus. Figure 4.8 displays the difference between the calculated and experimental level energies, for the different Coulomb contributions. The pure GXPF1 result is also included. The figure shows that when the different Coulomb interaction contributions are included, the accuracy of the calculation decreases, which is a bit of a surprise.

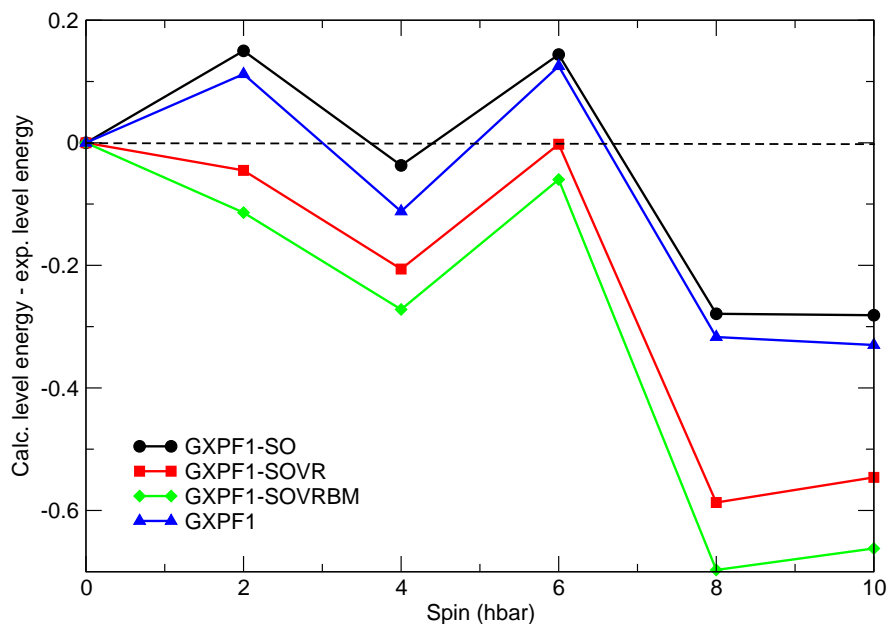


Figure 4.8: The difference between the calculated and experimental level energies, including varying Coulomb effects. Only even spin yrast states are considered, and up to 6p-6h excitations were allowed. The discrepancy between the calculated and experimental level energies increases when the isospin symmetry breaking effects are included.

The black curve is obtained by using the GXPF1 interaction modified to include the electromagnetic spin orbit interaction. Considering that the $1f_{7/2}$ ($2p_{3/2}$) orbital corresponds to a $j = l + s$ orbit and that its partner is the $1f_{5/2}$ ($2p_{1/2}$) orbit corresponding to $j = l - s$, the spin orbit coupling can be an important factor in the nucleus, since excitations between these orbits is usual.

The red curve in Fig. 4.8 is calculated by including a radial term, V_r in addition to the electromagnetic spin orbit interaction. The radial term, sometimes called the Thomas-Ehrman shift, corresponds the change of the radius when the nucleons are excited from one orbit to another. The excitation will affect the charge distribution of the nucleus, and this in turn changes the level energies in the nucleus. The V_r contribution is sensitive to if protons or neutrons are excited. Both the electromagnetic spin orbit term and the radial term are discussed in more detail in Ref. [13]. The green curve in Fig. 4.8 includes the electromagnetic spin orbit interaction, the radial term and a charge symmetry breaking term, BM . The BM term corresponds to a charge symmetry breaking component of the strong force, i.e., the strong force does not affect the protons and neutrons equally. Strictly seen this effect is not a Coulomb effect, but like the Coulomb force it breaks isospin symmetry. The charge symmetry breaking term is discussed at length in Ref [30] and is therein shown to be present in several fp shell nuclei. However, including it in this calculation increases the deviation from the experimental results.

It is possible that Fig. 4.8 reflects the difficulties in separating the different forces inside the atomic nucleus. This is especially important since GXPF1 is an interaction partially fitted to experimental level energies. These experimental data are taken from nuclear levels created by a combination of the strong force and Coulomb force. Hence it is possible that the original GXPF1 interaction already contains an implicit dependence on the Coulomb force. Thus, to explicitly include Coulomb effects by changing the single-particle energies and two-body matrix elements, too large effect are simulated. This could be the explanation for the decreasing accuracy of the calculation as the Coulomb effects are included.

To further investigate this phenomenon, the level energies were calculated for the KB3G interaction including the Coulomb interaction. The result is presented in Fig. 4.9. On average the difference between the calculated energy levels and the experimental level energies decreases when the isospin symmetry breaking effects are included in the KB3G interaction. Consequently, by including these effects here the experimental results are relatively better reproduced. While KB3G includes experimental single-particle energies and a small mass dependence, it is not fitted to experimental ground-state energies or level energies as GXPF1 is. This implies that it in some sense is a more 'pure' interaction than GXPF1. The results showed in Fig. 4.9 could be taken as evidence for this.

A currently popular field of research in nuclear structure physics are mirror nuclei. Mirror nuclei have their number of protons and neutrons interchanged, for instance $^{57}_{29}\text{Cu}_{28}$ and $^{57}_{28}\text{Ni}_{29}$. If the strong force is considered to be charge independent, the only difference between excited states in a mirror pair, should be due to the Coulomb force. It is not uncommon to study Coulomb effects in mirror nuclei

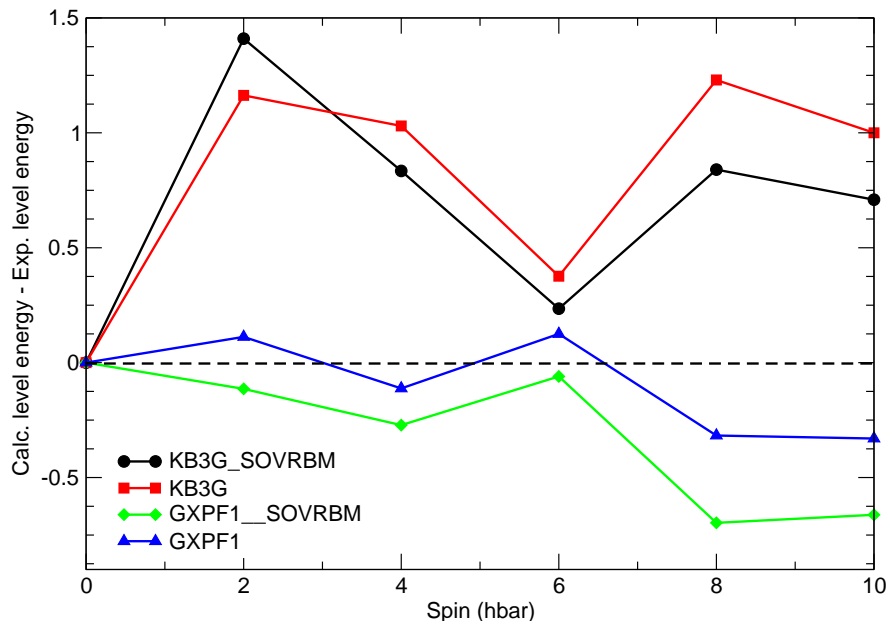


Figure 4.9: The difference between the calculated end experimental level energies, for the KB3G and GXPF1 interaction both with and without Coulomb effects. The agreement between the calculated and experimental level energies increases when the isospin symmetry breaking effects are included for KB3G.

with the help of shell model calculations, sometimes using GXPF1 including various Coulomb effects. Considering the above results, the benefit of studying mirror nuclei with GXPF1 both with and without Coulomb effects is questionable.

4.2.5 Transition probabilities

Using ANTOINE the electromagnetic transition probabilities were derived. The reduced transition probabilities, the $B(E2)$ and $B(M1)$ values were calculated using the bare g -factors. The g_s and g_l are 5.586 respective 1.0 for protons and -3.826 respective 0.0 for neutrons. Standard effective charges of $1.5e$ and $0.5e$ for protons and neutrons respectively were used. The use of standard effective charges rather than effective charges will not change the results, as no Coulomb effects were considered in these calculations. Hence, the wave functions are completely symmetric for the proton and neutron partitions. The branching ratios, b , were calculated using the above. The results are presented in table 2 of paper 1, where the experimental and theoretical branching ratios are given. The theoretical values were obtained from a calculation using $t = 6$ and the GXPF1 interaction without any Coulomb effects included. As seen in the table the experimental branching ratios are very well described by the theoretical calculation but with one very notable exception: The calculation fails to predict the feeding and decay pattern of the yrast and yrare 8^+ states.

The yrast and yrare 8^+ states

To the left in Fig. 4.10 a section of the experimental level scheme is shown and in the middle is the level scheme predicted by the shell model calculation using GXPF1. Obviously a significant difference exists between the experimental and theoretical level schemes. However, the theoretical level scheme displayed to the very right in Fig. 4.10 is very similar to the experimental level scheme.

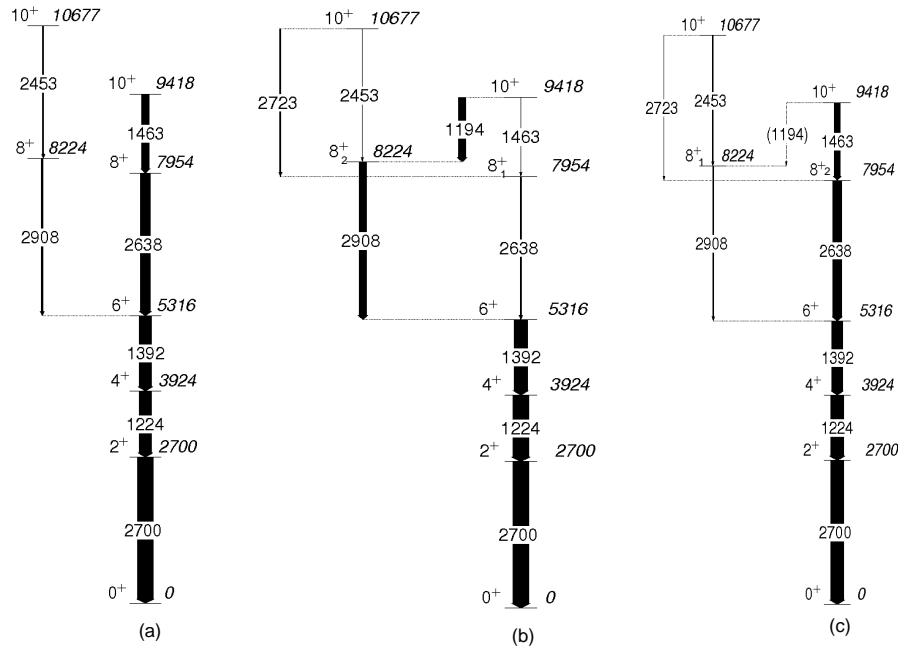


Figure 4.10: Panel (a) displays the relevant section of the experimental level scheme and panel (b) displays the decay pattern given by the shell model calculation. To the very right, panel (c) displays the level scheme obtained when the yrast experimental level is associated with the second calculated 8_2^+ and vice versa.

This level scheme was obtained by associating the experimental yrast 8^+ state with the second calculated 8^+ state and vice versa. It thus seems like the shell model calculation places the experimental yrast 8^+ state as the second calculated 8^+ state and vice versa. The reason for this inversion is due to the wave function of the 10_1^+ which prohibits an $E2$ transition into 8_1^+ but allows an $E2$ transition into 8_2^+ , this is discussed further in Paper 1.

Several calculations have been performed to investigate if this failing is specific for the GXPF1 interaction, or if it persists for KB3G as well, the results are presented in Tab. 4.1. Table 4.1 also includes branching ratios obtained from a calculation using GXPF1a. The branching ratios were calculated from results obtained by Ref. [31] using $t=8$ without any Coulomb effect included. Though the inversion of the yrast and yrare 8^+ states still remain, GXPF1a reproduces the experimental decay pattern very accurately. It has been reported that the inversion of the 8^+ states still exists for a full fp shell calculation using GXPF1a in Ref. [29].

E_γ (keV)	I_i^π (\hbar)	I_f^π (\hbar)	E_γ (keV)	b_{exp}	b_{theo} GXPF1	b_{theo} KB3G	b_{theo} GXPF1a
5316	6_1^+	4_1^+	1392	1.0	1.0	1.0	<i>n.a.</i>
7954	8_2^+	6_1^+	2638	0.94(1)	0.92	0.94	0.93
		6_2^+	1304	0.07(1)	0.08	0.05	0.07
8224	8_1^+	6_1^+	2908	1.0	0.52	0.10	0.94
		6_2^+	1574	<i>n.o.</i>	0.37	0.62	0.06
		7_1^+	623	<i>n.o.</i>	0.11	0.28	<i>n.a.</i>
9418	10_1^+	8_1^+	1194	<i>n.o.</i>	0.00	0.03	0.01
		8_2^+	1463	1.0	0.99	0.97	0.99
10677	10_2^+	8_1^+	2453	1.0	0.73	0.21	0.88
		8_2^+	2723	<i>n.o.</i>	0.15	0.04	0.10
		9_1^+	1667	<i>n.o.</i>	0.06	0.57	<i>n.a.</i>
12359	12_1^+	10_1^+	2940	0.75(3)	0.86	0.58	<i>n.a.</i>
		10_2^+	1681	0.25(3)	0.12	0.05	<i>n.a.</i>
		11_1^+	938	<i>n.o.</i>	0.01	0.37	<i>n.a.</i>

Table 4.1: Comparison between the experimental and theoretical branching ratios, b , for GXPF1, KB3G using $t=6$, and a $t=8$ calculation performed by Ref [31] using GXPF1a. These branching ratios were calculated assuming the inversion of the 8^+ yrast and yrare states. Clearly all calculations invert these two states. The calculation using GXPF1a obtains results most similar to the experimental values. The branching ratios marked *n.o.* were not observed in the present analysis, and transitions marked *n.a.* were not available from Ref. [31].

The inversion of the 8^+ states remains for the KB3G calculation as well. This is clearly seen in the branching ratio of the calculated 10_1^+ state. It is noteworthy that KB3G cannot reproduce the decay pattern of the 12_1^+ state, nor the decay of several of the other states.

Transition probabilities using KB3G

The branching ratios for the KB3G interaction were used to produce a predicted level scheme of ^{56}Ni . The relevant part of it is shown in Fig. 4.11. Clearly the experimental decay pattern is not well reproduced by the KB3G interaction, for states above spin parity 6^+ . Especially noteworthy is the predicted decay of the 11_1^+ state and the 10_2^+ , which typically decay with strong $E2$ transitions, but here prefer $M1$ transitions. The same is valid for the 12_1^+ transition which has a much stronger decay branch into the 11_1^+ level than the second 10_2^+ level, which again favours the $M1$ transition over the $E2$ transition. To investigate this, the configurations creating these excited states were studied. In Tab. 4.12 the dominating configurations for some excited states are shown. The reason behind the peculiar decay pattern predicted by KB3G is seen in the table. For instance the dominating configuration forming the 12_1^+ state has two holes in $1f_{7/2}$ and two particles in $1f_{5/2}$. This configuration has the strength 33% in the 10_1^+ state and only 11% in the 10_2^+

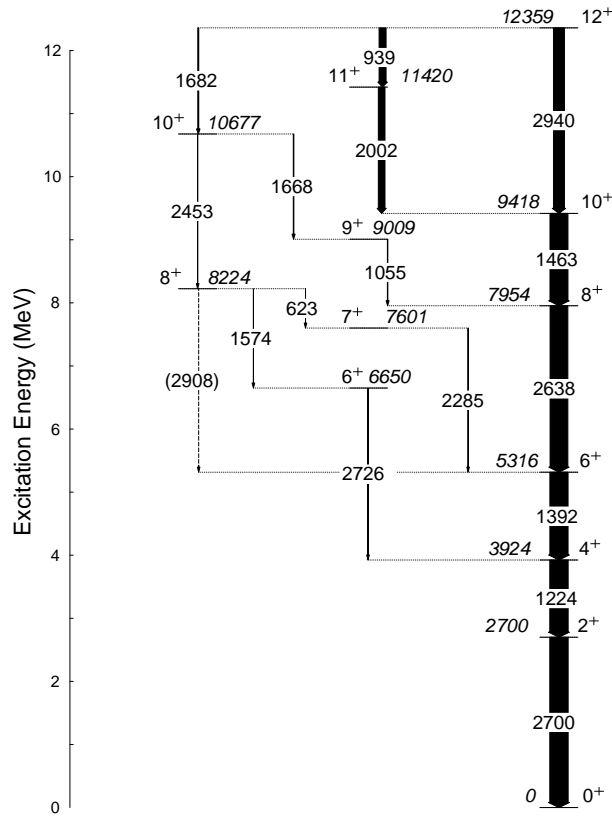


Figure 4.11: The decay pattern of ^{56}Ni as predicted by the shell model calculation using KB3G. Clearly the experimental decay pattern is not well reproduced.

Interaction	State I^π	Fraction %	$1f_{7/2}$	$2p_{3/2}$	$2p_{1/2}$	$1f_{5/2}$
KB3G	12_1^+	61	14	0	0	2
	11_1^+	49	14	0	0	2
	10_1^+	33	14	0	0	2
	10_2^+	24	14	1	0	1
		15	14	2	0	0
		11	14	0	0	2
	9_1^+	24	14	1	0	1
		15	14	2	0	0
	4	14	0	0	2	
GXPF1	12_1^+	17	13	2	0	1
	11_1^+	20	14	0	0	2
	10_1^+	25	14	0	0	2
	10_2^+	21	13	3	0	0
	9_1^+	19	14	2	0	0

Figure 4.12: The fractions for the dominating configurations for some levels in ^{56}Ni , calculated with the KB3G interaction. The dominating configurations for the same states calculated by GXPF1 are also included. The wave functions are symmetric in their proton neutron partitions as the Coulomb force was not included in these calculations.

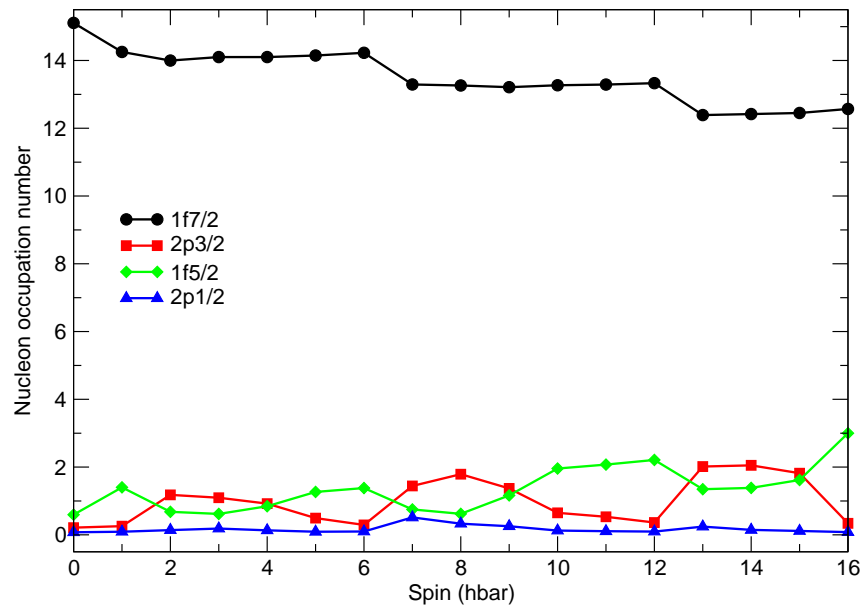


Figure 4.13: The nucleon occupation number for the different fp orbitals calculated using KB3G. Comparing these results to the occupation numbers obtained from GXPF1 in Fig. 4.6, it is seen that the $1f_{5/2}$ orbital is more favoured using KB3G than GXPF1.

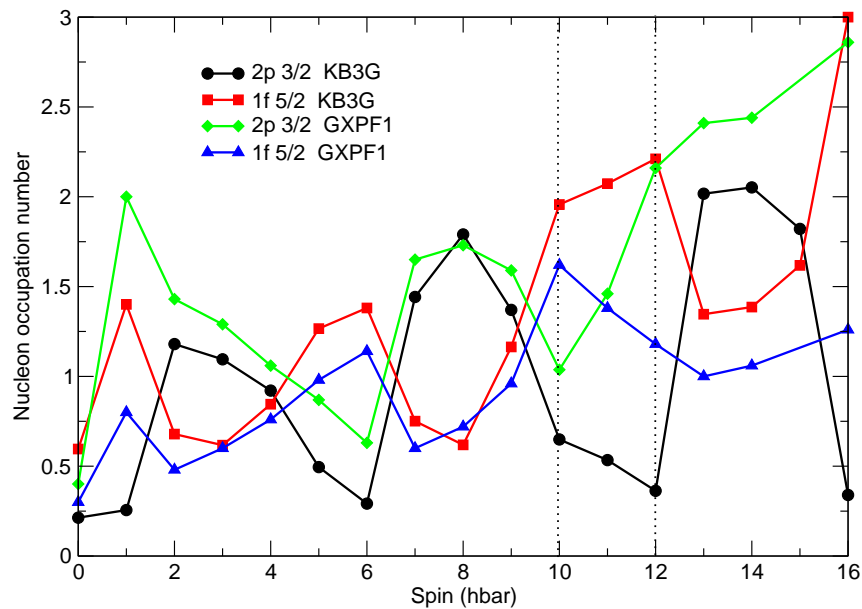


Figure 4.14: The nucleon occupation number for the $1p_{3/2}$ and $1f_{5/2}$ orbitals calculated using KB3G in the black respective the red curve, using GXPF1 in the green curve respective the blue curve. The region enclosed by dotted lines displays the greatest discrepancy between the predicted occupation numbers for the two interactions.

state. However, the 11_1^+ is to 49% made up of this configuration. Thus it is more favourable to decay into the 11_1^+ state than the 10_2^+ state. The same argument can be used to explain the decay of the 11_1^+ into the 10_1^+ state, the dominating configurations are the same for these two states. The 9_1^+ however, only has 4% of their leading configuration.

Comparing the configurations from KB3G and GXPF1, it is seen that the dominating configuration is predicted to be the same only for the 10_1^+ and 11_1^+ states. According to KB3G the 12_1^+ state has a very strong component of 61% of two holes in $1f_{7/2}$ and two particles in $1f_{5/2}$. The same state, has according to GXPF1 a much more mixed wave function, with a leading configuration of only 17% consisting of three holes in $1f_{7/2}$, two particles in $2p_{3/2}$ and one particle in $1f_{5/2}$. The largest difference in the leading configurations for the states displayed in Tab. 4.12 all seems to involve the $2p_{3/2}$ and $1f_{5/2}$ orbitals.

In Fig. 4.13 the occupation numbers for the fp orbitals using KB3G are shown. Comparing this figure to the corresponding Fig. 4.6 obtained by using GXPF1, it is seen that the $1f_{7/2}$ occupation numbers are quite similar for the two interactions as well as the occupation of the $1p_{1/2}$ orbital. However, the occupation of the $1p_{3/2}$ and $1f_{5/2}$ orbit are different in the two calculations. To highlight this, the occupation of the $2p_{3/2}$ and the $1f_{5/2}$ orbitals are included in Fig. 4.14 calculated by either KB3G or GXPF1. While the numerical values for the occupation differs in the two results, the general behaviour of the occupation numbers is almost alike, except for $I^\pi = 10^+$, 11^+ and 12^+ . For instance, the predicted occupation of the $2p_{3/2}$ decreases (increases) for KB3G (GXPF1) between $10^+ \leq I^\pi \leq 12^+$.

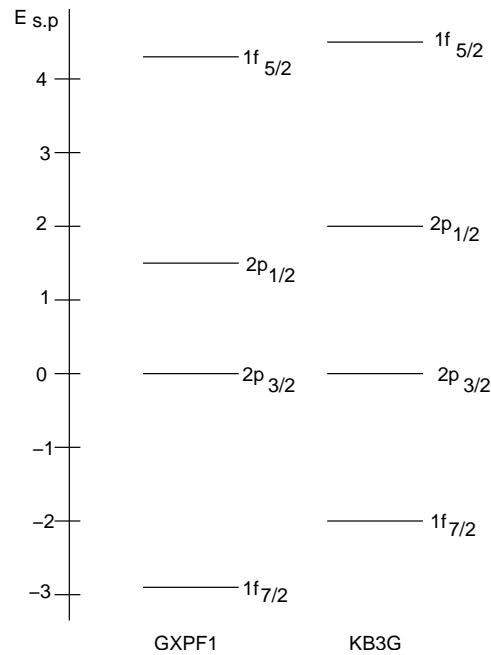


Figure 4.15: The single-particle energies used in the GXPF1 and KB3G interaction, in MeV.

The significant difference between the predicted level schemes using KB3G and GXPF1, can depend on both the single-particle energies and the two-body matrix elements. The single-particle energies for KB3G and GXPF1 are illustrated in Fig. 4.15. The figure shows that the single-particle energies in KB3G are more 'compressed' than in GXPF1. To promote a particle from $1f_{7/2}$ to $2p_{3/2}$ in GXPF1 (KB3G) some 2.9 (2.0) MeV is necessary. This could be the explanation why the dominating configurations calculated by GXPF1 favours excitation into the $2p_{3/2}$ more than KB3G does. It is also noteworthy that the biggest difference between the single-particle energies between GXPF1 and KB3G exists precisely for the $2p_{3/2}$ orbital. So for the KB3G interaction to achieve a high level energy it is necessary to excite nucleons into the $1f_{5/2}$ orbital, whereas GXPF1 can excite into the $2p_{3/2}$ orbital and still have enough excitation energy. However, as the occupation numbers for most of the other state show a similar behaviour for all orbitals and in both calculations, perhaps the problem is not in the single-particle energies, but rather in the two-body matrix elements. Here the solution of the problem may lie in the two body matrix elements between the $1f_{7/2}$ and $2p_{3/2}$ respective $1f_{5/2}$ orbitals.

The reason for the poor reproduction of the experimental results for KB3G requires further theoretical work as does the peculiar inversion of the yrast and yrare 8^+ states which persists for the KB3G, GXPF1, and GXPF1a interactions even for a full fp shell calculation [29].

Chapter 5

The Lund University Silicon Array

In experiments using fusion evaporation reactions many different residual nuclei are produced. To clearly and unambiguously identify the reaction products, detection and identification of evaporated particles is crucial. This was one of the reasons why a state of the art charged particle detector, LuSiA - the Lund University Silicon Array - was created.

The other reason was a new fascinating decay mode displayed by some nuclei in the $A \sim 60$ region, namely the so called prompt particle decay (c.f. Sec. 2.3). This decay has been observed in nuclei produced in fusion-evaporation reactions, where highly deformed or even superdeformed mother nuclei decay by emitting protons or α particles of discrete energies, into near spherical states in the daughter nuclei. To detect with high accuracy both the energy and angle of the protons and α particles, LuSiA has a large angular coverage and a high granularity. LuSiA was first utilised during a heavy ion fusion-evaporation reaction experiment (c.f. 3.3), in this chapter the design and calibration of LuSiA is discussed.

5.1 The strip detectors

LuSiA is a system of eight $\Delta E - E$ silicon strip telescopes. The use of $\Delta E - E$ telescopes enables discrimination between different kinds of charged particles, for example protons, deuterons, and α particles. The E detectors were bought from the company RADCON. They have active areas of $61 \text{ mm} \times 61 \text{ mm}$ in size and are approximately 1 mm thick. The E detectors have 32 strips which are mutually combined to yield 16 electronic channels. The ΔE detectors are based on the LASSA type [32] and were purchased from the company MICRON. They are $50 \text{ mm} \times 50 \text{ mm}$ in size, about $65 \mu\text{m}$ thin with 16 strips.

The surface of silicon detectors is covered by a dead layer consisting of aluminium. The dead layer on the ΔE detectors is $\sim 0.2 \mu\text{m}$ thin. The E detectors have nominally 0.5 (1.9) μm dead layers on its front (back) side. The ΔE and E detectors are arranged together in a specific geometry to form the Lund University Silicon Array - LuSiA.



Figure 5.1: (a) The silicon wall consisting of four $\Delta E - E$ telescopes. (b) The box detector holder and silicon wall placed inside the target chamber, without any telescopes placed in the holder for the box. Notice that the target holder is placed inside the box. (c) Trying to fit all of the cables inside the target chamber for the full LuSiA array and two rings of the Microball detector.

5.2 Detector arrangement

LuSiA is designed to fit inside the target chamber at the germanium detector array Gammasphere [19]. Gammasphere is currently placed at the Argonne National Laboratory outside of Chicago in the United States of America. In essence, LuSiA replaces the charged particle detector Microball [20].

Four of the eight telescopes form the so called wall. The wall, seen in panel (a) in Fig. 5.1, covers the forward angles $5^\circ < \Theta < 40^\circ$. The other four telescopes form the so called box. The box, seen in panel (b) and (c) of Fig. 5.1, covers the central section around the target ($40^\circ < \Theta < 120^\circ$). The most backward angles, i.e. $130^\circ < \Theta < 170^\circ$ were covered by a remaining, small section of Microball, which is also seen in panel (c) of Fig. 5.1. This set-up is ideal for reactions in inverse kinematics, which means that a heavier projectile nucleus impinges on a target con-

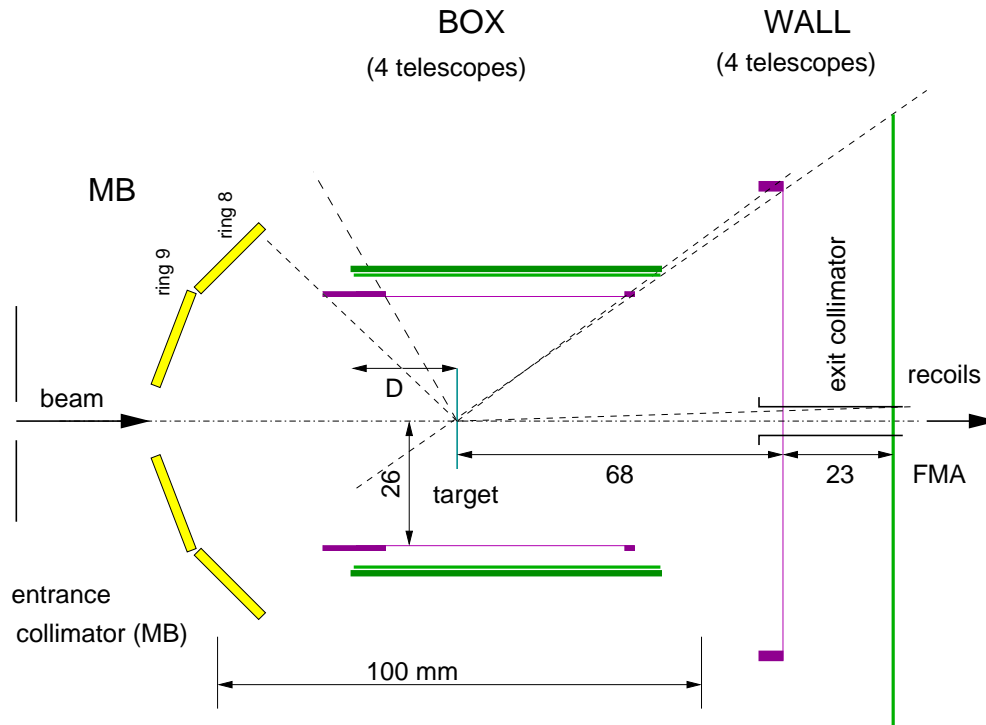


Figure 5.2: The set-up of LuSiA at Gammasphere with two rings from Microball shown in yellow. The $\Delta E(E)$ detectors are shown in purple (green). The beam enters from the left, hits the target and the reaction products exit through the exit collimator into the Fragment Mass Analyser (FMA). Picture courtesy of D. Rudolph.

sisting of lighter nuclei. This causes the reaction products to be strongly forward focused due to the conservation of momenta. Hence it is intended that the prompt protons primarily will be detected by the wall.

A code to simulate the response of LuSiA to evaporated particles from a given reaction was developed. It estimates the charged particle detection efficiency depending on the geometry defined by the relative position of the target and the box, D , and the energy thresholds of the ΔE and E detectors. The parameter D is displayed in the center of Fig. 5.2.

If $D = 0$, the target and box are lined up such that the box covers angles less than 90° . To place the target in the middle of the box, D has to be 2.5 cm. The energies and angles of the evaporated particles were taken from a preceding Monte Carlo simulation of the reaction process. In panel (a) of Fig. 5.3 the minimum detection energies of protons and α -particles are displayed, for $E_{threshold}(\Delta E) = 0.2$ MeV and $E_{threshold}(E) = 0.5$ MeV and $D = 1.5$ cm for pixels at $\Phi \sim 20^\circ$ as a function of Θ . The discontinuity in the curves at $\Theta \sim 40^\circ$ corresponds to the transition between the box and the wall. The minimum detection energy in the laboratory frame for protons (α - particles) is almost constant at ~ 4 MeV (~ 15 MeV). In the center-of-mass frame this corresponds to increasing particle energies, as is seen in the figure. The dashed horizontal lines illustrate typical center-of-mass energies for the prompt particle decays. In this set-up, the detection region for them is from $\Theta \sim 40^\circ$ to

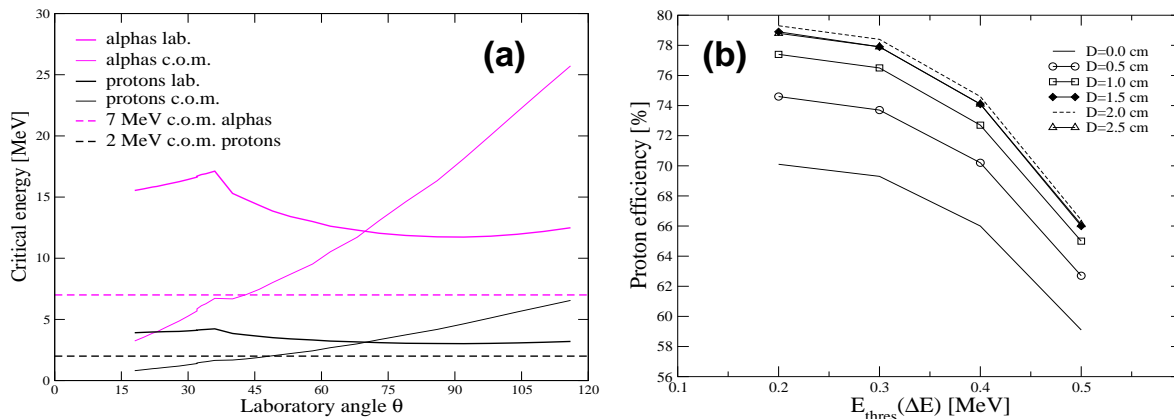


Figure 5.3: (a) The critical energy of α particles (purple curves) and protons (black curves) for the lab system and the center of mass (c.o.m) system. (b) The detection efficiency for protons for varying target positions, as a function of the threshold energy of the ΔE detector. Picture courtesy of D. Rudolph.

$\sim 90^\circ$. In Fig. 5.3 (b) the simulated proton detection efficiencies as a function of the energy thresholds of the ΔE detector for a number of distances is shown. For protons the distance $D = 2.0$ cm provides the highest proton detection efficiency, whereas for α particles (not shown in Fig. 5.3 (b)), smaller values of D are preferable. A reasonable compromise between the two results in $D = 1.5$ cm.

The results from the simulations form the basis for the geometrical set-up of LuSiA used in the present experiment. A side view of this set-up is shown in Fig. 5.2 with the beam entering from the left. The ΔE detectors are shown in purple and the E detectors are illustrated in green. The two rings of Microball (MB) are shown in yellow to the left in the picture. Not included in this figure are the absorber foils, which are placed in front of the ΔE detectors during the experiment. The absorber foils protect the detectors from being hit by heavy high energy particles, as these damage the detectors. The absorber foils are further discussed in Sec. 5.6.5. The holding structure of the LuSiA detectors is based on the Microball bar. It has been developed and machined at Lund University and at Washington University in St. Louis, U.S.A. LuSiA was mechanically put together at Washington University.

In the present configuration LuSiA has $8 \times 2 \times 16 = 256$ electronic channels. These can be combined to form $8 \times 16 \times 16 = 2048$ pixels. In Fig. 5.4 the pixels of the box and wall are displayed. Note that some of the pixels are hidden. For instance some pixels in the wall are hidden by the box or by the holding frame of the wall, as it is shown in Fig. 5.4. Some 1850 of the 2048 pixels were geometrically active for detection of charged particles.

The high granularity of LuSiA makes it possible to precisely determine the momenta of the evaporated particles and subsequently the momenta of the recoiling nuclei prior to possible prompt particle decay. It is important to accurately know

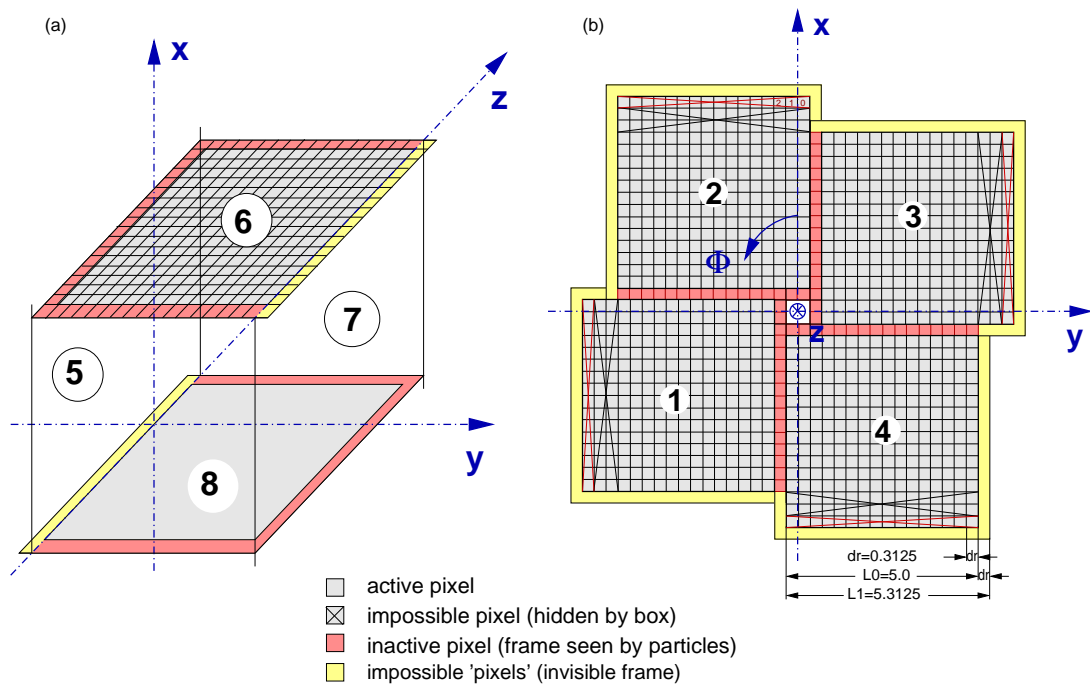


Figure 5.4: Schematic view of the telescopes of the box in panel (a) and the wall in panel (b). Active pixels are indicated in grey. The pixels in the wall which are geometrically hidden by the box are crossed over, and pixels shadowed by the frames of the printed circuit boards (PCB) are shown in pink. The yellow parts indicate the frames of the PCB, which in addition are shadowed from direct hits of particles. Picture courtesy of D. Rudolph.

the recoil vector in order to properly transform the particle and γ - ray energies measured in the laboratory system to the center of mass system. In fusion-evaporation reactions, the spin axis of the produced nuclei is perpendicular to the plane spanned by the beam axis and the recoil vector. This allows an event by event determination of the spin axis which is vital for the study of angular distributions of the promptly emitted particles.

5.3 Electrical set-up

Silicon detectors are semiconductor detectors consisting of crystalline materials. When an ionising particle passes through the detector material electron-hole pairs are created. The great advantage of these detectors is that the energy necessary to liberate an electron-hole pair is very small. Thus, for a given energy many more information carriers (electron-hole pairs) are created in this detector than in most other types. This leads to a superior energy resolution. The electron-hole pairs are separated from each other by an applied external electrical field. The electrons are swept away to the anode and the holes to the cathode. The size of the signal is proportional to the amount of ionisation caused by the incident radiation. The signals obtained from silicon detectors are very small, thus it is necessary to pream-

plify them before further processing. The preamplifier is ideally mounted as close as possible to the detector (in order to minimize noise).

The signals from the ΔE and E detectors of LuSiA are taken out from the target chamber by flat cables, which can be seen in the upper right part of Fig. 5.1 in panel (c). In this picture, the funnel used to guide the flat cables out from the target chamber is also visible. The preamplifiers are housed inside a small tower, just outside of the Gammasphere holding structure. The connectors of the flat cables are glued to the PCB preamplifier boards in a vacuum feed-through. This is necessary to not destroy the vacuum inside the target chamber. The signals from the LuSiA preamplifiers are then sent to the Gammasphere electronics room via shielded flat cables and processed there by a special 16-channel shaper unit produced at Washington University. The shaper unit derives both energy and time signals from the incoming pre-amplified signals. These signals are digitised in the 16-channel ADC and TDC unit, and sent in to the Gammasphere data acquisition system. During the experiment LuSiA is used in a so called slave mode. This means that when the trigger conditions are fulfilled the information from LuSiA is read out. LuSiA does not contribute to the trigger set-up. Typically during the experiment 3 (c.f. Sec. 3.3) a combination of neutron and γ -ray signals was used as a trigger.

5.4 Determination of the angles of the pixels

The pixels are created by combining the electric channels from one ΔE and one E detector together. The E strips are rotated 90° with respect to the ΔE strips, thus creating pixels. Given the position of one pixel, the angles (Θ, Φ) for all pixels can be determined. The position of the pixels is described by the Cartesian coordinate system. The origin of the coordinate system is the target or, more specifically, the beam spot in the center of the target.

To illustrate the process of determining the angles for the pixels, the upper left telescope in the wall is used as an example in the following discussion. The ΔE and E detectors are placed at different distances with respect to the target (see panel (a) of Fig. 5.5): the ΔE detectors are placed at $z = 68$ mm from the target and the E detectors are placed even further out. The first step is to project the position of the E detectors onto the position of the ΔE detectors. This is important because, for our example, the x position is given by the strips in the ΔE detector and the y position is conversely given by the E detector strips. The z coordinate is the position of the ΔE detector from the target, i.e. $z = 68.0$ mm. To properly create pixels from these conditions, the E detectors have to be mathematically projected onto the position of the ΔE detectors:

- The position of the first pixel depends on the middle position of the first strip in the (i) ΔE detector, (ii) E detector and (iii) the ΔE distance from the target. The middle position of the first E strip is projected onto the position of the ΔE detector through;

$$y_1 = -8.10 \cdot \frac{68.0}{85.4} \text{ mm} = -6.45 \text{ mm}$$

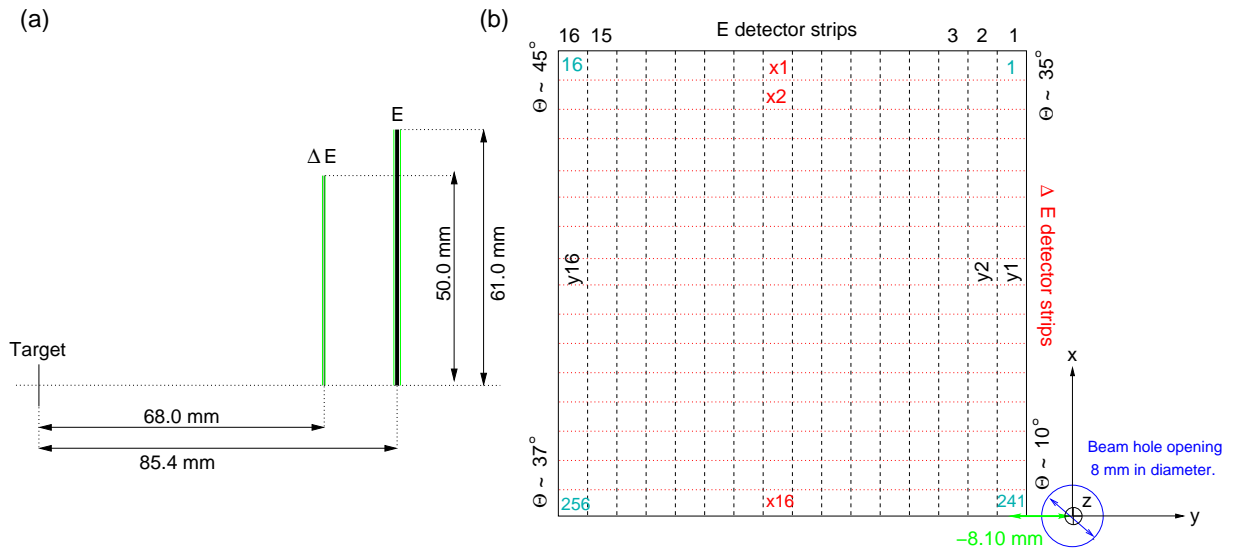


Figure 5.5: (a) For the top left detector in the wall, the ΔE detector is placed 68 mm from the target and the E detector is placed 17.4 mm further out. (b) The pixels are created by combining the strips from the ΔE detector, shown in red, and the E detector shown in black.

where the factor -8.10 mm corresponds to the distance in y direction from origo to the middle of the first E strip, see Fig. 5.5 panel (b). The distance 68.0 (85.4) mm corresponds to the distance from the target to the ΔE (E) detectors (see Fig. 5.5 (a)).

- As the ΔE detectors have active areas of 50.0 mm and 16 strips, the width of each strip in the x - direction is $\Delta x = 3.13$ mm. The corresponding value for the E detectors, which have an active area of 61.0 mm, is 3.81 mm. However, seen from the ΔE detector position this number is modified to:

$$\Delta y = 3.81 \cdot \frac{68.0}{85.4} \text{ mm} = 3.04 \text{ mm}$$

Thus the effective pixel size at the ΔE position is 3.13 mm \times 3.04 mm.

Utilising these parameters it is possible to generate all the pixels through a code. The position of the first pixel is used as the starting point. The first pixel in the upper left telescope of the wall is displayed in turquoise in panel (b) of Fig. 5.5. The code takes steps in, for instance, the y direction which are 3.04 mm long until the middle of the last strip in the detector is reached. The program then jumps down 3.13 mm and steps another 16 steps which are 3.04 mm long and this continues all over the detector. In this fashion the pixels of LuSiA were determined, each of the eight telescopes consists of 256 pixels.

Once the x , y , and z positions of the pixels were known, the angles can be calculated by using the transformation from the Cartesian coordinates to the spherical

coordinates:

$$\begin{aligned}x &= r \sin\Theta \cos\Phi \\y &= r \sin\Theta \sin\Phi \\z &= r \cos\Theta\end{aligned}$$

It is necessary to know the angles for the pixels in order to properly calibrate LuSiA and determine the momenta of the evaporated particles during the experiment (cf. Sec. 5.2). The calibration of LuSiA was performed in many steps described in Secs. 5.5 and 5.6. The calibrations utilise both an α decaying source and a beam of protons impinging on a ^{12}C target.

5.5 The alpha calibration

The α calibration was performed individually for the ΔE and E detectors. This is due to the very short range of α -particles in matter. The ΔE detectors had to be physically removed from the experimental set-up to enable the α particles to impinge on the E detectors. However, the ΔE detectors in the box are very sensitive and the mechanical set-up too delicate to be removed. Thus, it was not possible to α -calibrate the E detectors in the box.

In the process of removing the ΔE detectors of the wall, one of the E detectors in the wall was damaged. Thus, no α calibration was obtained for the lower right E detector in the wall either.

Two transition energies from the decay of a ^{228}Th source were utilised for the calibration, namely the 5685.37 keV transition from ^{224}Ra and the 8784.86 keV transition from ^{212}Po . These two transitions are suitable to calibrate after since they are intense and span the energy region of interest well. When the α -particle transverses the dead layer on top of the detector it will lose some energy. Therefore it has a lower energy than the tabulated value when it enters the active area of the detector. How much energy the α particle loses in the dead layer depends on its initial energy and on the thickness of the dead layer. The latter will in turn depend on the incident angle of the α particle.

To illustrate this effect, the upper left telescope in the wall is again chosen as an example. The effective thickness, t_{eff} , of the dead layer in the wall is described by:

$$t_{eff} = \frac{t}{\cos\Theta}$$

The nominal thickness, t , of the dead layer on the front side of the E - detectors in the wall is $0.5 \mu\text{m}$. The angle Θ varies over the detector area. It even varies within the same strip, which is indicated in Fig. 5.5 (b). There pixel 1 and 241 are marked together with their angles $\Theta_1 = 35^\circ$ and $\Theta_{241} = 10^\circ$. They belong to the same E strip but the effective thickness for pixel 1 is:

$$t_1 = \frac{0.5 \mu\text{m}}{\cos 35^\circ} = 0.61 \mu\text{m}$$

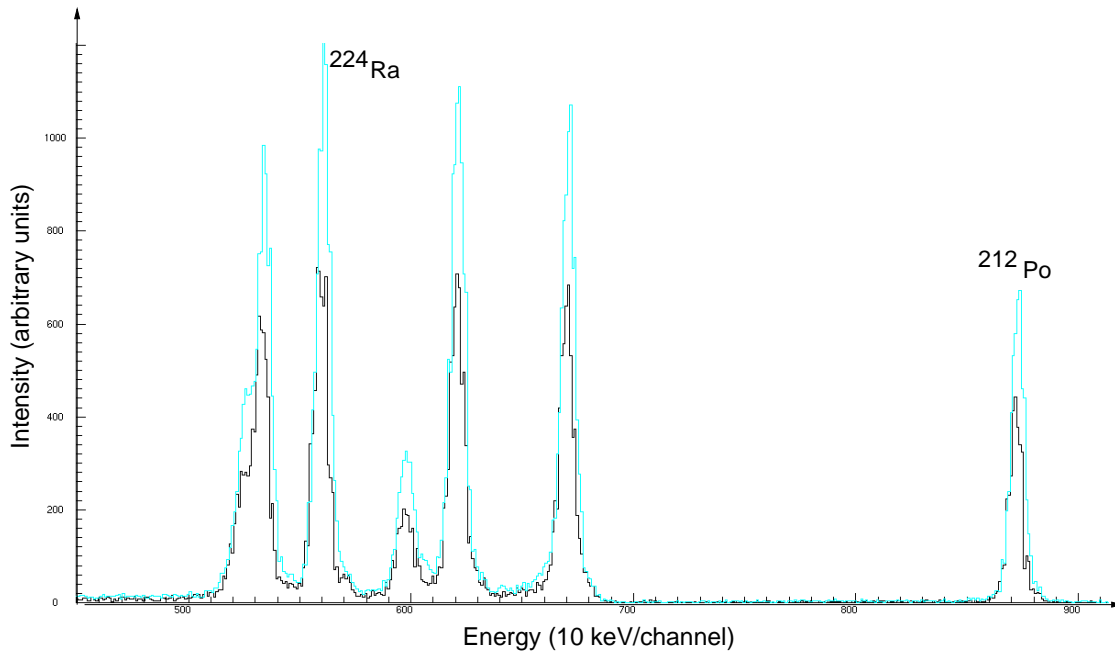


Figure 5.6: The α calibration source, ^{228}Th decays (among other) into ^{224}Ra and ^{212}Po . The energies of these two transitions were used for the calibration. Here seen for two E detector strips (number 4 and 13, cf. Fig. 5.5) in the upper left wall.

and the effective thickness for pixel 241, t_{241} , is $0.51 \mu\text{m}$.

An α particle with an initial energy of 7.00 MeV will lose 68 (81) keV in the 0.51 (0.61) μm thin dead layer, i.e., α -particles with different energies will strike the active area of the detectors.

It is impossible to know event-by-event where the α particle struck the strip. Therefore the energy of the α particle is not well known and an average angle, $\bar{\Theta}$, for each strip was determined, corresponding to the angle of the middle of the strip. The average angle for the strips was used to calculate the average energy loss, \bar{E}_{loss} , by the α particles in the dead layer. The energy loss of α particles in the dead layers was calculated by the code SRIM [33] (cf. Sec. 5.6 for an example of this). The average energy deposited in the active area of the detector, \bar{E}_{det} , is thus:

$$\bar{E}_{det} = E_{tabulated} - \bar{E}_{loss}$$

For strips far out in the detector the variation in Θ decreases as seen Fig. 5.5 (b). Hence the approximation of an average angle works better for this region.

The energies deposited in the strips by the α - particles were recorded. Together with the nominal energy, \bar{E}_{det} calculated above, these were used to obtain the α calibration coefficients (a_i , b_i) corresponding to a linear curve. For each strip the coefficients transform the measured channel, C , into energy according to $E_\alpha = C \cdot a_i + b_i$.

A calibrated spectrum of the ^{228}Th source is displayed in Fig. 5.6 for two E strips in the upper left detector in the wall. The small difference between the positions of the peaks in the two spectra is due to the different energy losses in the dead layers,

the turquoise (black) curve corresponds to E strip number 4 (13) in Fig. 5.5.

Prompt protons typically have a kinetic energy of about 7 MeV in the laboratory system at the forward angles. Thus the energy region of interest is well spanned by the α calibration for the E detectors. Given the same energy, protons have a considerably longer range in matter than α particles. Thus, a proton with a kinetic energy of 7 MeV will not be stopped in the ΔE detector. These protons will pass through the ΔE detector and hit the E detector, where they will be stopped. Typically they deposit 0.4 - 0.9 MeV in the ΔE detector and the remaining energy is deposited in the E detector. It cannot be taken for granted that the energy response over this energy interval (from ~ 0.4 MeV to ~ 8 MeV) is linear. Thus a proton calibration is necessary to calibrate the ΔE detectors for low energies.

5.6 Proton Calibration

The proton calibration proved more difficult than the α calibration. The main problem was difficulties in focusing the beam and steering it through the 8 mm opening hole in the LuSiA wall. This opening hole can be seen to the right in Fig. 5.2. These problems caused the number of recorded protons for the calibration to be small. Two proton calibrations were performed; with and without absorber foils placed in front of the ΔE detectors. The first step in the proton calibration is to determine the expected energy of the protons for a given pixel.

5.6.1 Determination of the proton energy

The proton calibration was performed by having a beam of protons impinging on a thin ^{12}C target. The protons either scatter elastically or inelastically on the target. This gives rise to protons of two discrete energies striking the detectors. The protons have an energy E_Θ according to;

$$\begin{aligned} E_\Theta &= (r + \sqrt{r^2 + s})^2, \quad \text{with} \\ r &= \frac{\sqrt{m_a^2 E_a}}{m_a + m_B} \cos\Theta \quad \text{and} \\ s &= \frac{m_B Q + E_a(m_B - m_a)}{m_a + m_B} \end{aligned} \tag{5.1}$$

where E_a is the initial energy of the protons (12 MeV), m_a is the mass of the proton, and m_B is the mass of the ^{12}C nuclei. For inelastic scattering the protons excite the ^{12}C nuclei into their first 2^+ state at an energy of 4.439 MeV. This is the Q value for this reaction, whereas for elastic scattering Q is zero. As can be seen in the above equations, the energy of the protons also depends on the scattering angle Θ . How to determine the angles for all of the pixels is described in sec. 5.4. Using the angles it is possible to calculate the expected energies of the scattered protons, for each pixel.

Notice though, that this energy depends on the initial energy of the protons, E_a . Just like the α particles, the protons will lose energy in the dead layer on top of the detectors. Thus the energy loss in the dead layers has to be determined, in order to know the energy deposited in the detectors. As mentioned before in Sec. 5.5, the effective thickness of the dead layers only depends on the nominal thickness, t , and the Θ angle for the wall. However, for the box the effective thickness depends on where the detectors are placed in relation to the target. The top and bottom telescopes, labelled number six and eight in Fig. 5.4, are parallel to the x -axis. The effective thickness is in this case given by

$$t_{eff} = \frac{t}{\sin\Theta\cos\phi}$$

The detectors placed to the left and right of the target, labelled telescopes five and seven in Fig. 5.4 are parallel to the y axis which yield an effective thickness of

$$t_{eff} = \frac{t}{\sin\Theta\sin\phi}$$

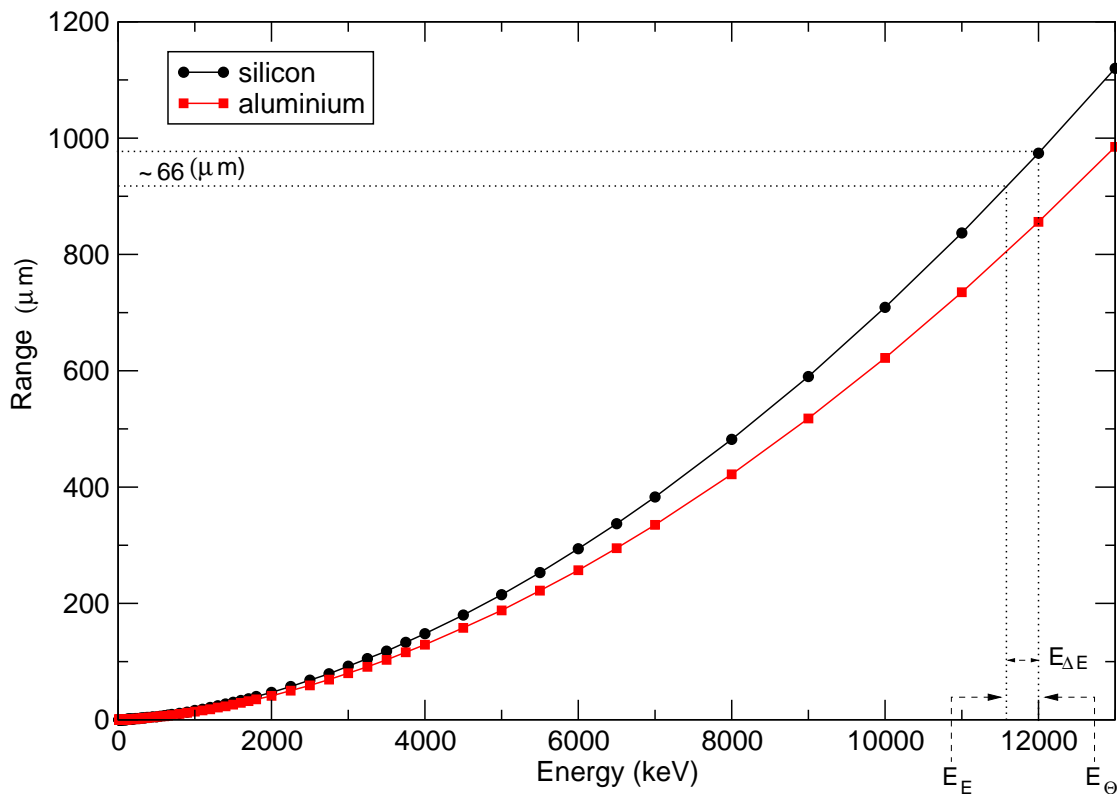


Figure 5.7: The range of protons in silicon (black curve) and aluminium (red curve) calculated by SRIM. By using the energy of the protons, E_Θ , their range can be determined.

The range of particles in matter depends on their energy. The range is not a linear function of energy. This is illustrated in Fig. 5.7 which shows the range of protons

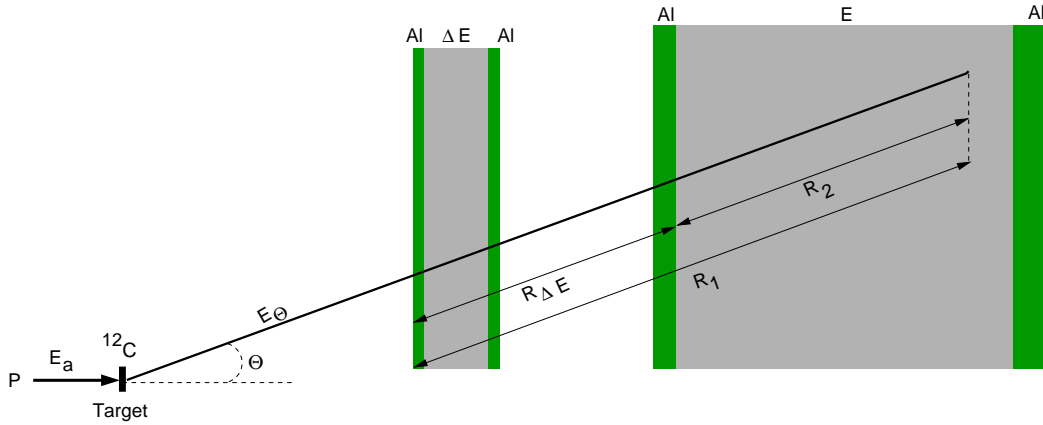


Figure 5.8: Schematic illustration (thicknesses not to scale) of the process to calculate the energy deposited in the ΔE and E detectors. The grey area corresponds to the silicon detectors and the green area, the dead layers. See text for further details.

in silicon (aluminium) in the black (red) curve, calculated by using SRIM [33]. The energy loss of charged particles in matter can be described by the reduced Bethe-Block equation

$$\frac{dE}{dx} \propto \frac{mZ^2}{E}$$

where m is the mass of the incoming particle, Z^2 its proton number, E is its energy and dE its energy loss over the distance dx . Over the same distance, a particle with low energy will lose more energy than an identical particle with more energy. The low energy particle will thus have a shorter range than the high energy particle. When calculating how much energy is supposed to be deposited in the ΔE and E detectors this non linear behaviour has to be taken into account.

The energy loss of protons in *thin* layers of silicon and aluminium is very similar, which also can be seen in Fig. 5.7. To simplify the calculations the energy losses by protons in silicon and aluminium were assumed to be indistinguishable. This allows the approximation that the ΔE detector is thicker, i.e., to its actual thickness of some $65 \mu\text{m}$ an additional $1 \mu\text{m}$ silicon was added. This corresponds to the thicknesses of the aluminium dead layers on the front and back side of the ΔE detectors as well as the front of the E detectors.

The following notations are illustrated in Fig. 5.8, showing the different layers a particle has to pass in order to hit the E detector. In Fig. 5.8 the silicon detectors are marked in grey and the dead layers are given in green. The energy of the protons depends on the scattering angle Θ and the range, R_1 , of the protons corresponding to this energy, E_Θ , was calculated using the function obtained from SRIM

$$R_1 = 5.29 \cdot 10^{-6} E_\Theta^2 + 1.77 \cdot 10^{-2} E_\Theta - 4.17 \quad (5.2)$$

which gives the range in the unit μm if the energy is in MeV. To determine how much of E_Θ is deposited in the ΔE detector and the dead layers, the length $R_{\Delta E}$ of

these has to be subtracted from R_1 according to

$$R_2 = R_1 - R_{\Delta E}$$

The range R_2 (cf. Fig. 5.8) corresponds to a certain energy, E_E , deposited in the E detector, which is calculated by using the function obtained from SRIM. Thus the energy deposited in the dead layers and the ΔE detector is

$$E_{\Delta E} = E_{\Theta} - E_E$$

Since only the total energy of the protons, E_{Θ} , is of interest, it does not matter that the energy loss in the dead layers is contained within the expression of $E_{\Delta E}$. This energy is used in the calibration, and hence the energy loss of protons in the dead layers is 'baked' into the calibration coefficients for the ΔE detector. The charged particles detected during the experiment must, of course, be treated in the same way. Once these energies have been determined, it is also possible to reconstruct the initial energy, E_a , of the protons detected in a certain pixel at angle Θ .

5.6.2 The beam energy

In the theoretical calculation to determine the proton energy, it is necessary to know the initial energy of the protons, E_a as defined in Eq. 5.1. A problem relating to this was discovered while investigating the energy deposited in the E detectors by protons using *only* the α calibration. The protons had more energy than they were expected to have.

During the experiment, the proton beam energy, E_a , was stated to be 12.00 MeV. However, after discussions with the beam operators at the ATLAS facility at Argonne National Laboratory, who provided the beam, it was concluded that the beam energy is never very accurately known. Accordingly the beam energy was by the beam operators given the uncertainty (12.0 ± 0.3) MeV.

However it is possible to determine the beam energy by measuring the energy of the protons only using the α calibration. For instance, the spectra displayed in the turquoise curve in Fig. 5.9 corresponds to the fourth strip in the upper left E wall for the proton calibration. The two peaks correspond to energies of 11.427 MeV and 6.750 MeV for the elastically and inelastically scattered proton respectively.

To know which beam energy these measured values correspond to the following steps were taken

1. Determine the thickness of the ΔE detector

The nominal thickness given for the upper left ΔE detector in the wall is 62 μm . The Θ angle for this strip is 23.7° , giving an effective thickness of

$$t_{eff} = \frac{62}{\cos 23.7^\circ} \mu\text{m} = 67.7 \mu\text{m}$$

2. Calculate the energy of the protons

The protons have energies, E_{Θ} , given by Eq. 5.1. If the beam energy, E_a , is 12.00

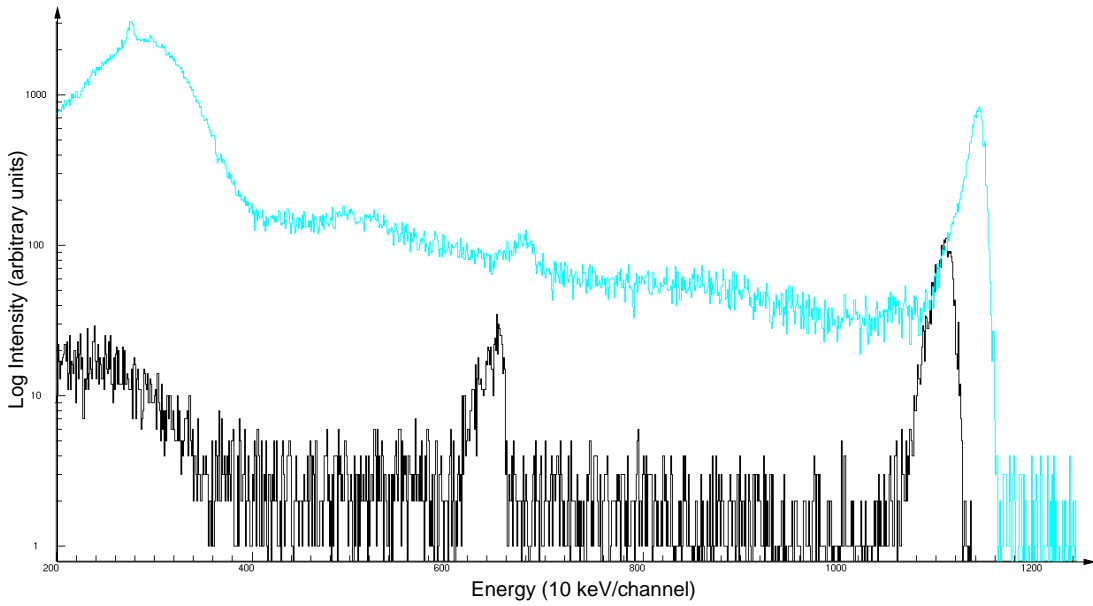


Figure 5.9: Spectrum for strip number 4 (13) in the turquoise (black) curve, in the upper left E detector in the wall, for the proton calibration. Notice the large difference in the background level for the two strips.

MeV the energies of the protons are 11.83 MeV and 7.38 MeV.

3. Energy in the E detector

The range of the protons in the silicon detectors is calculated by using the formula 5.2 obtained from SRIM with the theoretical proton energies. Thus the range of the elastically scattered proton becomes

$$R_1 = (5.29 \cdot 10^{-6} \cdot 11.83^2 + 1.77 \cdot 10^{-2} \cdot 11.83 - 4.17) \mu\text{m} = 946.1 \mu\text{m}$$

and for the inelastically scattered proton it becomes

$$R'_1 = (5.29 \cdot 10^{-6} \cdot 7.38^2 + 1.77 \cdot 10^{-2} \cdot 7.38 - 4.17) \mu\text{m} = 414.7 \mu\text{m}$$

This is the full range of the protons corresponding to their energy. To know how much of this energy which is deposited in the E detector, the range, R_2 has to be determined.

$$R_2 = R_1 - R_{\Delta E}$$

where $R_{\Delta E}$ includes the thickness of the ΔE detector, the dead layers of the ΔE detector and the front dead layer on top of the E detector. In this example we hence have

$$R_2 = 946.1 \mu\text{m} - 67.7 \mu\text{m} = 878.4 \mu\text{m}$$

and

$$R'_2 = 414.7 \mu\text{m} - 67.7 \mu\text{m} = 347.0 \mu\text{m}$$

To calculate the energy corresponding to this range, Eq. 5.2 can be solved to reveal the energy, E_E

$$E_E = \frac{-1.77 \cdot 10^{-2} \pm \sqrt{(1.77 \cdot 10^{-2})^2 + 4 \cdot 5.29 \cdot 10^{-6}(878.4 - 4.17)}}{2 \cdot 5.29 \cdot 10^{-6}} = 11.350 \text{ MeV}$$

and

$$E'_E = \frac{-1.77 \cdot 10^{-2} \pm \sqrt{(1.77 \cdot 10^{-2})^2 + 4 \cdot 5.29 \cdot 10^{-6}(347.0 - 4.17)}}{2 \cdot 5.29 \cdot 10^{-6}} = 6.645 \text{ MeV}$$

which is the energy deposited in the E detector for the ranges R_2 and R'_2 .

Comparing these theoretically calculated values to the experimental values of 11.427 MeV and 6.750 MeV, we do not see a good agreement. However, if we assume that E_a is 12.07 MeV, and perform the above calculations again, we achieve an energy deposited in the E detector of 11.421 MeV and 6.720 MeV. For this initial energy of the protons the deviation between the calculated and the theoretical values are 6 keV respectively 30 keV, which were the smallest deviations found. Therefore the beam energy, E_a is determined to be 12.07 MeV for the present experiment, and the theoretical proton energies needed to calibrate the detectors are calculated using the new beam energy of 12.07 MeV.

5.6.3 Spectra

The above mentioned steering problems of the beam during the calibration runs caused serious problems. The count rate in the strips, especially in the ones close to the beam center ($x=y=0$) was very high, causing significant pile-up. Pile-up occurs when two (or more) events are being processed by the detector and the associated electronics at practically the same time.

Two typical proton calibration spectra are shown in Fig. 5.9, where the turquoise (black) curve corresponds to strip number 4 (13) in the upper left E detector of the wall. Clearly strip 4 is heavily influenced by pile-up and it is difficult to unambiguously identify the peak corresponding to the inelastically scattered proton. For strip 13 (in the black curve) the general background is much lower, but so is the statistics in the peaks as well.

To obtain cleaner spectra for the calibration, matrices over the energy loss in the ΔE detector versus the energy in the E detector were created. These are shown in panels (a)-(c) of Fig. 5.10 for the upper left telescope in the wall. The effect of pile up is clearly seen in panel (a). The expected appearance is a matrix with two discrete points (as the protons have discrete energies) but clearly the measured data displays something quite different. Panel (a) holds the total collected statistics during the proton calibration runs. It is very noisy and it is difficult to clearly identify the two proton peaks. The corresponding matrix for one selected pixel is shown in panel (b), where the noise is substantially reduced. For the calibration, further conditions were placed on the energy signals; the energy deposited in the ΔE and E detectors had to full-fill the conditions;

$$\begin{aligned} 0.3 \text{ MeV} &\leq E_{\Delta E} \leq 1.1 \text{ MeV} \text{ and} \\ 5.5 \text{ MeV} &\leq E_E \end{aligned}$$

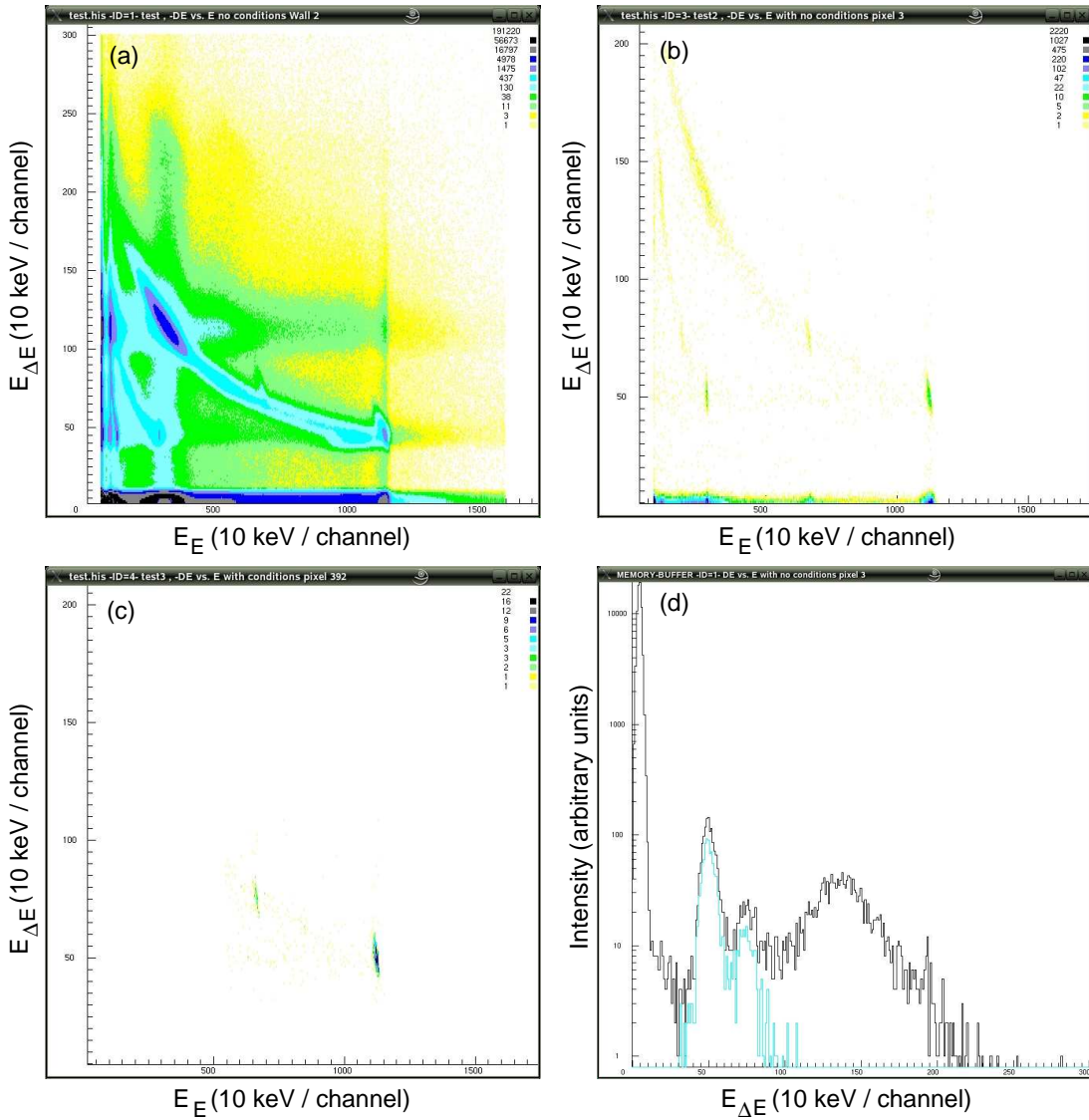


Figure 5.10: Panel (a) through (c) show ΔE versus E matrices for the proton calibration. Panel (a) includes the entire collected statistics for the upper left telescope in the wall. Panel (b) displays the collected statistics for one selected pixel in the wall, and panel (c) is the result of imposing some energy conditions on panel (b). The projection of the matrices in panel (b) and (c) onto the ΔE axis is shown in panel (d) in black respectively turquoise curves.

The result of imposing these conditions is shown in panel (c), which reveals two proton points.

In panel (d) the spectra obtained by projecting the matrices onto the ΔE -axis for panel (b) (black curve) and panel (c) (turquoise curve) are presented. The calibration was performed by using the energy of the elastic peak (i.e. the peak with lower energy) obtained from the turquoise curve, because this spectrum is cleaner. The black curve also contains a few more peaks, corresponding to random coincidences between noise and the protons.

To avoid using the strips with large pile up for the calibration, pixels with good and unambiguous statistics were used. The energy deposited in these pixels were assumed to represent the energy deposited in the strip. The proton calibration is also performed per strip, i.e. one pixel per strip is sufficient to calibrate it.

5.6.4 Calibration

The proton energy deposited in the E - detectors was measured. It corresponds to a certain theoretically calculated energy. By utilising this, the coefficients for a linear calibration curve can be obtained. For the E detectors which had no α calibration (cf. Sec. 5.5), the coefficients to a two point linear curve were derived. The green curve in Fig. 5.11 is an example of a calibration curve for a strip in a wall detector. Also in Fig. 5.11 the α calibration for the same strip in the wall is displayed in the

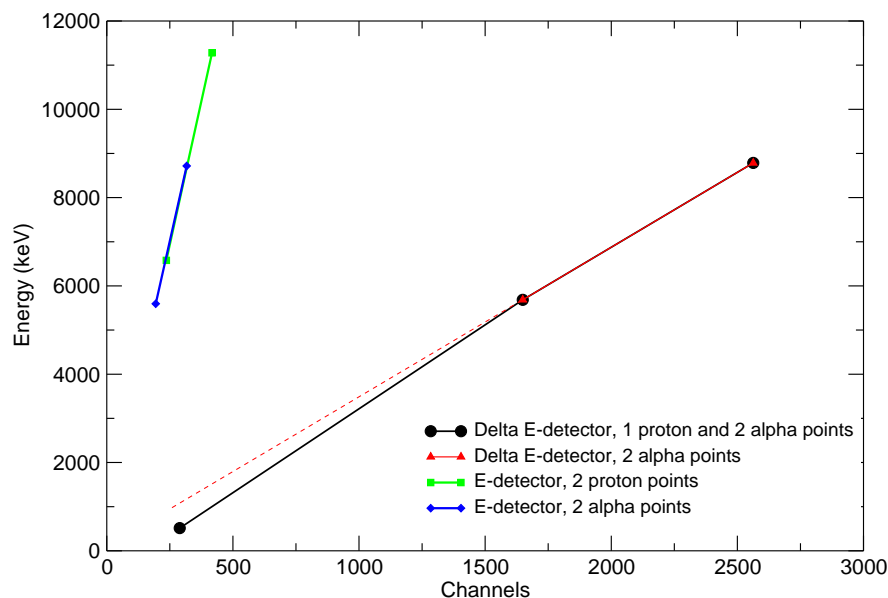


Figure 5.11: Calibration curves for the ΔE detector, using one proton and two α points in the black curve, and in the red curve only two α points are used. The calibration curves for the E detector is shown in green (two proton points) and blue (two α points). The need for a non-linear calibration for the ΔE detectors is apparent when comparing the black and red dotted curves.

blue curve, evidently the two calibrations are practically identical.

The energy deposited in the ΔE detectors for the protons was also measured. Typically the protons leave 0.4 to 0.9 MeV in the ΔE detector. Therefore the calibration for the ΔE detector must be able to describe the entire energy region from low energy (~ 0.4 MeV) to high energy (~ 8 MeV). The calibration for the ΔE detectors employs both α calibration points and a proton calibration point. Only one of the proton peaks was used, as the statistics for the inelastically scattered proton is lower than for the elastically scattered proton. This is seen in panel (d) of Fig. 5.10. With the measured values and the theoretical energies, the coefficients to a second degree polynomial curve were derived. These translate the measured channels, C , into energy, E , according to $E = a_i \cdot C^2 + b_i \cdot C + d_i$.

The calibration curve for one of the ΔE strips is shown in black in Fig. 5.11. This calibration curve is only slightly parabolic. Nonetheless compared to a linear calibration only using the α calibration points shown in the red dotted line, a clear difference exists between the two curves, especially at low energies. Consequently, it reinforces the need to include the proton point in the calibration of the ΔE detectors for low energies.

5.6.5 Absorber foils

To protect the detectors from being struck by heavy high energy particles during the experiment, absorber foils are placed in front of the ΔE detectors. The absorber foils consisted of tantalum and aluminium of varying thicknesses, illustrated in Fig. 5.12, for the box in panel (a), the wall in panel (b) and a photo of the wall absorbers in panel (c). Any particle, which enters the detectors during the experiment, first has

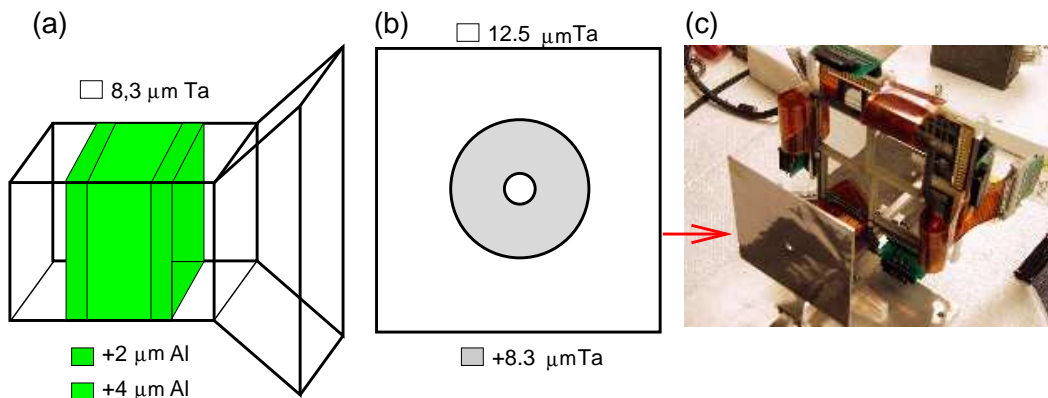


Figure 5.12: The absorber foils for (a) the box and (b) wall, displaying the varying materials and thicknesses in μm . In panel (c) the wall absorber foil is displayed.

to pass through the absorber foils. Naturally some of the particle energy is deposited in the absorbers. To determine how much energy is lost by the particle, yet another proton calibration was performed but with the absorber foils in place. This proton calibration was identical to the proton calibration described in Sec. 5.6. Since the proton energy in both calibrations was the same, the decrease in energy deposited

in the detector is directly proportional to the thickness of the foils.

The procedure is described in the following numerical example:

For a pixel in the lower right corner of the upper left telescope of the wall, the energy deposited in the detector before (after) the absorbers were inserted was 12.080 (11.490) MeV. Using the SRIM formula Eq. 5.2, as above, their range was determined as 266.03 (244.92) μm . The difference in range is $(266.03 - 244.92) \mu\text{m} = 21.11 \mu\text{m}$, i.e., the effective thickness of the foil. This pixel is placed at an angle of $\Theta=13.2^\circ$, giving a nominal thickness of $21.11/\cos 13.2^\circ = 20.6 \mu\text{m}$. This value is indeed very similar to the value given by the manufacturer of $20.8 \mu\text{m}$, as seen in panel (b) of Fig. 5.12. When the absorbers are placed in front of the ΔE detectors, the energy deposited in the detectors is not the total energy of the protons. Naturally this is due to the energy loss in the absorber foils. To determine the proper energy of the protons, the energy loss in the foils has to be compensated for. This correction will depend on where the pixel is placed, how thick the absorber in front of it is. Again using the example of the upper left wall in the telescope; the absorber foil is placed at $z = 62 \text{ mm}$, from the target, thus it needs to be projected on to the position of the ΔE detectors. In Fig. 5.12 panel (b) the radius, r , of the $20.8 \mu\text{m}$ thick area is 3.25 cm , but seen at the ΔE detector position, its actual size is 3.57 cm , according to

$$r_{eff} = 68 \cdot \frac{3.25}{62} \text{ cm} = 3.57 \text{ cm}$$

Thus all protons impinging on the detectors within this area have to pass $20.8 \mu\text{m}$ of tantalum. Using the energy deposited in the ΔE and E detectors it is possible to calculate the range, R_1 of the protons as described in Sec. 5.6.1. By adding the angle dependent thickness of the absorbers foil to R_1 , the energy of the protons *before* hitting the absorber foils can be determined. By performing this correction it is possible to treat the energy deposited in the detector as if there were no absorbers in front of them.

5.7 Evaluation of the calibration

To study the accuracy of the calibration the initial energy, E_a of the protons was calculated by using the measured energies deposited in the detectors, i.e., E_Θ as defined in Eq. 5.1, properly compensated for the energy loss in the absorber foils. In Fig. 5.13 the pixels of the upper left telescope in the wall are shown on the y - axis versus E_a on the x - axis.

As expected two discrete points can be seen for each pixel. The pixel ordering in this picture follows the notation introduced in Fig. 5.5. The first pixels, number one to 16, are placed in the first row of the upper part of the telescope. The subsequent pixels are placed lower and lower in the telescope, with increasing pixel number. As is seen in Fig. 5.13 the background increases a lot for pixels with high numbers. For these pixels a second high energy peak appears. Perhaps its origin is pile-up. The beam energy, E_a , which now should be constant for all pixels displays a peculiar behaviour. It decreases for pixels far out to the side of the detector. It can be explained if the size and/or the angle of the incoming beam spot is slightly misplaced. Implying that the pixels angles are not correct, as the origin of the coordinate system used to determine the pixels is the beam spot on the target. To achieve the

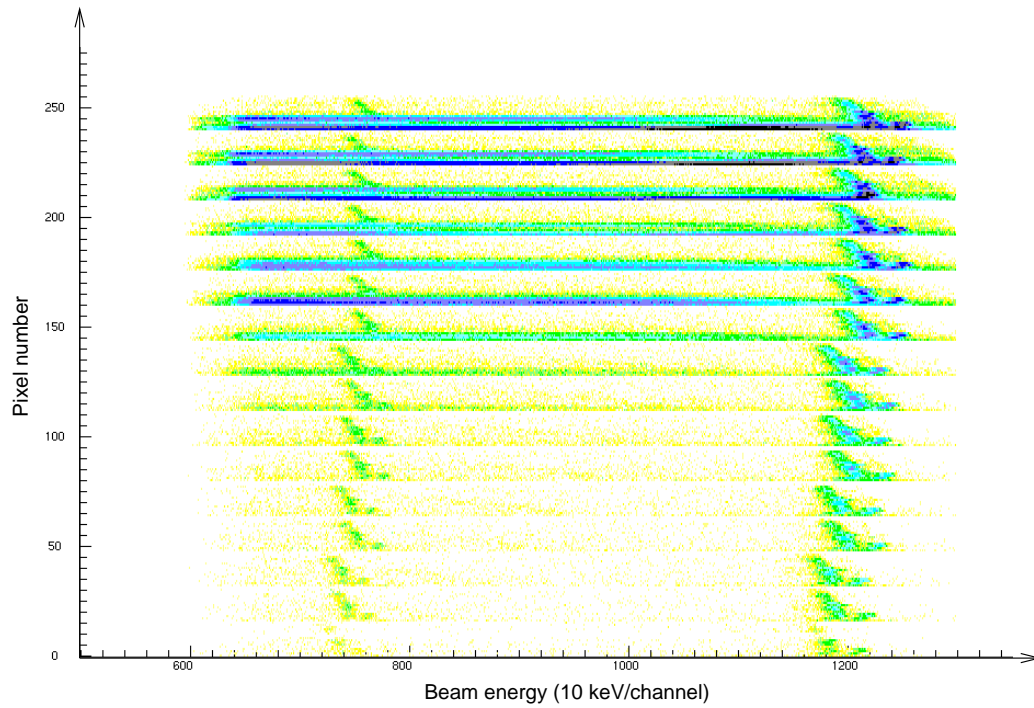


Figure 5.13: The beam energy of the protons for all pixels in the upper left telescope of the wall.

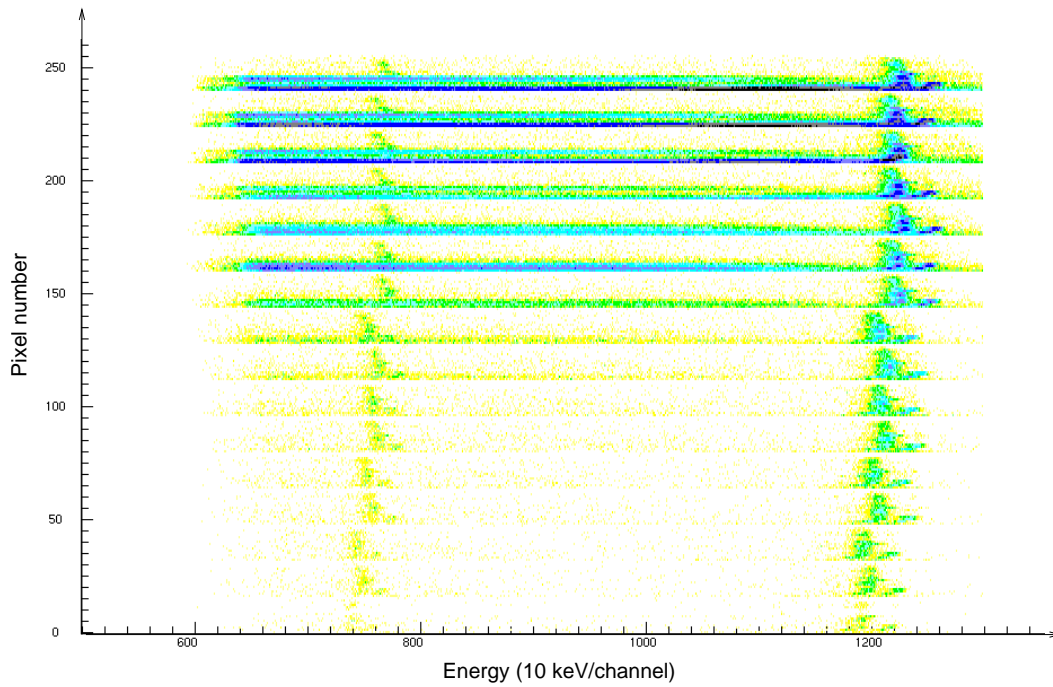


Figure 5.14: Modified beam energy of the protons for all pixels in the upper left telescope of the wall. See text for details.

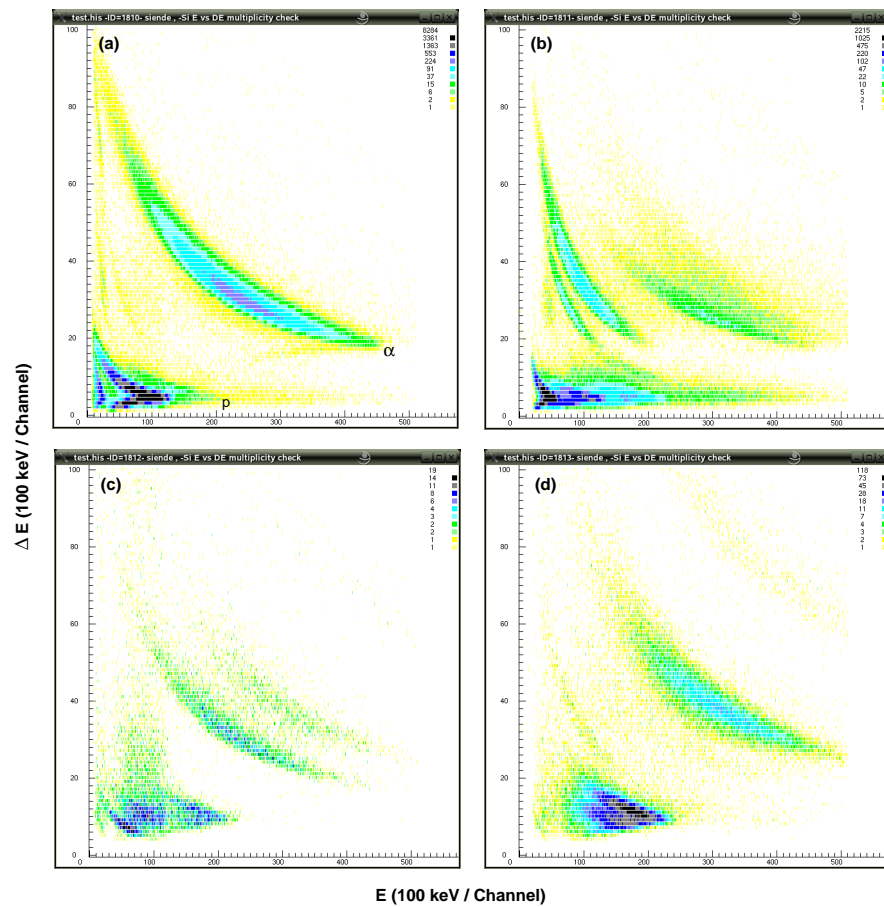


Figure 5.15: The energy deposited in the ΔE detector versus the energy deposited in the E detector. In panel (a) events with multiplicity one are shown, i.e., one hit in the ΔE detector and one in the E detector. In panel (b) events with one hit in the ΔE detector and two hits in the E detector. Panel (c) displays double hits in the ΔE detector and single hits in the E detector. Events with double multiplicity are shown in panel(d).

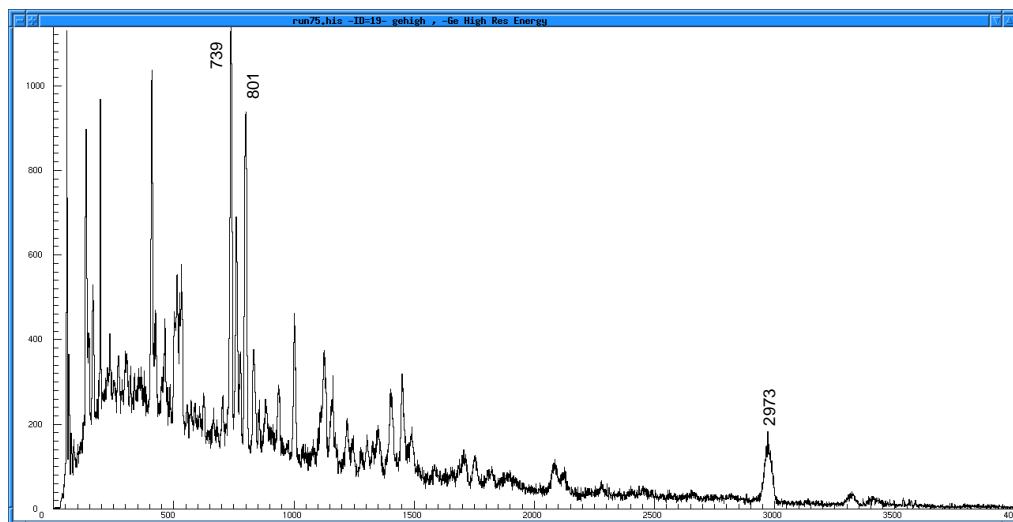


Figure 5.16: γ -ray spectrum of ^{55}Co obtained from experiment 3 using multiplicity one in LuSiA. Some of the previously known transitions in ^{55}Co are marked out.

correct behaviour for the beam energy a correction was introduced. The correction adds a constant number to beam energy, shifting it to the correct position. The result is displayed in Fig. 5.14 where the beam energy is displayed for each pixel. It is with this last correction nearly constant for all pixels.

At the moment of writing (November 2006) it is not possible to fully evaluate the calibration. If Fig. 5.14 had display two straight lines, the calibration would have been optimum, clearly the actual calibration is less than optimum. Currently the complete sort program for experiment 3 (c.f Sec. 3.3) to handle all of the signals from the detectors is being constructed. Some very preliminary data from experiment 3 is shown in Fig. 5.15, where the energy deposited in the ΔE detector versus the energy deposited in the E detector is shown. Panel (a) displays the spectra obtained if only one hit is demanded in both detectors. Panel (b) is obtained with one hit in the ΔE and two hits in E , panel (c) displays events with two hits in ΔE and one in E . Panel (d) have double multiplicity in both detectors. In panel (a), the protons and α -particles are clearly seen. Requiring multiplicity one in both the ΔE and E detectors, a γ -ray spectrum corresponding to a certain reaction channel can be created. In Fig. 5.16 the γ -ray spectrum from the $2\alpha 1p$ channel is displayed, corresponding to the residual nucleus ^{55}Co , and in the figure some of the previously known γ -rays are marked out.

The first goal of LuSiA to achieve a good particle identification is evidently meet. If the angular distribution and energy of the prompt particles can obtained from the present experiment remains to be seen.

Chapter 6

Conclusions and Outlook

An extended experimental level scheme of the doubly magic nucleus ^{56}Ni has been created. A comparison between the experimental results and large-scale shell-model calculations was performed. The two interactions used in the model gave very different results. The GXPF1 interaction can accurately reproduce the level energies in ^{56}Ni as well as its electromagnetic decay pattern, with one notable exception: it can surprisingly not reproduce the feeding and decay pattern of the yrast and yrare 8^+ states. The reason for this was traced to the wave functions of the involved levels, which inhibits the experimentally observed decay pattern. The KB3G interaction on the other hand, cannot predict the level energies or the electromagnetic decay properties of ^{56}Ni very well, except for some low energy yrast states. The Coulomb interaction was included in both calculations. This increased the accuracy of calculation using KB3G, whereas it decreased using GXPF1. The reason behind this behaviour requires future theoretical efforts. Pure particle-hole excitations were also studied, revealing the presence of single particle and rotational states in the experimental level scheme of ^{56}Ni .

The ground state of ^{56}Ni seems to be made up of 15 nucleons in the lowest possible state with one additional nucleon 'excited', already in the ground state. Possibly this is an indication that the $1f_{7/2}$ orbital below $N = Z = 28$ shell gap and the upper fp orbitals are not well separated in energy, i.e. that ^{56}Ni is not a good doubly magic nucleus. This is also indicated by that the excitation energy of the first 2^+ state is rather low compared to other doubly magic nuclei.

Almost all doubly magic nuclei have a 3^- state at relatively low excitation energy. This state corresponds to an octupole (pear shaped) vibration of the nucleus. However, in ^{56}Ni no indications of it were found in the present analysis. It is intended to perform an experiment specifically aimed at finding this missing level, as it would give an opportunity to study the competition between single-particle states and a collective excitation.

One of the most complex fusion-evaporation reaction experiments has been performed using a state-of-the-art charged particle detector, LuSiA. The calibration of LuSiA has proven to be very sensitive to small previously neglected aspects. It is also very easily affected by the beam energy, where a difference of 0.07 MeV between the given and the real value for the beam energy caused the initial calibration to fail.

The data handling of experiment 3 (c.f. Sec. 3.3) is in the process of being finalised. It is expected that the subsequent data analysis will provide unprecedented information on the angular distribution and energy of particles emitted in the prompt particle decay.

The doubly magic nucleus ^{56}Ni will be studied in the data set taken from experiment 3 in order to further extend the experimental level scheme which allows for a greater test of the shell model calculations. Another nucleus to be studied is ^{58}Ni . A total of 9 prompt proton decays and two prompt α decays have been suggested for ^{58}Ni [34]. The angular distribution of the prompt protons and α particles, could lead to a refined knowledge of single-particle orbitals inside deformed potentials and possibly the time it takes for the particle to tunnel through the nuclear potential barrier, i.e., the tunnelling *time*. This is of great scientific interest, not 'only' in nuclear physics but for physics and the natural sciences in general.

Acknowledgements

First of all, I would like to thank my supervisor, Dirk Rudolph, without whom this work would not have been possible. Your scientific curiosity is a true source of inspiration. I am also grateful for the hours you have spent helping me. My assistant supervisor Claes Fahlander's help with assorted physics 'problems' is also greatly appreciated.

To my constant office mate, Lise-Lotte Andersson, I am indebted for many hours of discussions and laughs. My new office mates Andreas Ekström and Diego Torres, are thanked for providing new perspectives on physics and life as a PhD student. A general thanks goes out to all members of the Nuclear Structure Group for providing a pleasant working atmosphere.

I would also like to thank all of my co-workers at the division of nuclear physics at Lund University for making every day at work enjoyable and for providing interesting coffee discussions.

I am also very appreciative of the people who have helped us with the experiments, both from Washington University and Argonne National Laboratory. The weekly nuclear coffee meetings are also appreciated for broadening my perspective on nuclear structure physics.

Finally, but equally important, I would like to thank my family and friends, for their support and love.

Bibliography

- [1] K. E. Johnson, Phys. perspect. 6 (2004) 295-309.
- [2] K. L. G. Heyde, "The Nuclear Shell Model", Springer Verlag, Heidelberg (1994).
- [3] M. Goeppert-Mayer, *On closed shells in nuclei II*, Phys. Rev. **75** (1949).
- [4] K.S. Krane, "Introductory Nuclear Physics", John Wiley & Sons, New York (1998).
- [5] <http://www.nndc.bnl.gov/nudat2/getdataset.jsp?nucleus=56NI>
- [6] <http://www.nndc.bnl.gov/nudat2/getdataset.jsp?nucleus=57NI>
- [7] E. Caurier, shell model code ANTOINE, IReS, Strasbourg 1989-2002.
- [8] E. Caurier and F. Nowacki, Acta Physica Polonica 30, 705 (1999).
- [9] A. Poves *et al.*, Nucl. Phys. A **694**, 157 (2001).
- [10] M. Honma, T. Otsuka, B.A. Brown, T. Mizusaki, Phys. Rev. C **65**, 061301 (2002).
- [11] M. Honma, T. Otsuka, B.A. Brown, T. Mizusaki, Phys. Rev. C **69**, 034335 (2004).
- [12] M. Honma, T. Otsuka, B.A. Brown, and T. Mizusaki, Eur. Phys. J. A **25**, s01, 499-502 (2005).
- [13] J. Ekman, C. Fahlander and D. Rudolph, Mod. Phys. Let. A **20**, 39, (2005).
- [14] M. A. Bentley and S.M. Lenzi, Prob. Part. Nucl. Phys. (2006).
- [15] R. du Rietz, PhD thesis, Lund University, ISBN 91-628-6394-0 (2005).
- [16] D. Rudolph *et al.*, Phys. Rev. Lett. **80**, 3018 (1998).
- [17] D. Rudolph *et al.*, Phys. Rev. Lett. **82**, 3763 (1999).
- [18] D. Strottman, N. Carjan, P. Talou, Phys. Scrip. T88, 148-152, (2000).
- [19] I.-Y. Lee, Nucl. Phys. A **520**, 641c (1990).
- [20] D.G. Sarantites *et al.*, Nucl. Instrum. Methods A **381**, 418 (1996).

- [21] <http://www.chemistry.wustl.edu/dgs/mball/images.html>
- [22] D.G. Sarantites *et al.*, Nucl. Instrum. Methods Phys. Res. Sect. A **530**, 473 (2004).
- [23] <http://www.phy.anl.gov/fma/>
- [24] <http://www.phy.anl.gov/fma/ic.html>
- [25] D. Torres, to be published.
- [26] L-L. Andersson, Licenciate thesis, Lund University, LUNFD6/(NFFR-3100)/1-69/(2006).
- [27] J. Ekman *et al.*, Phys. Rev. C **66**, 051301(R) (2002).
- [28] C. Andreoiu *et al.*, Eur. Phys. J. A **14**, 317 (2002).
- [29] M. Horoi *et al.*, Phys. Rev. C . **73**, 061305(R) (2006).
- [30] A.P. Zuker *et al.*, Phys. Rev. Lett. **89**, 142502 (2002).
- [31] M. Horoi, private communication.
- [32] B. Davin *et al.*, Nucl. Instrum. Methods A **473** (2001) 302-318.
- [33] <http://www.srim.org/#SRIM>
- [34] D. Rudolph, private communication.